Department of Precision and Microsystems Engineering

A system level performance analysis method for the design of a C-shape hexapod leg operating on compactive terrain

J. van Rijn

Report no   : 2022.014
Coach   : Dr.ir. J.F.L. Goosen
Professor   : Dr.ir. J.F.L. Goosen
Specialisation   : Engineering Mechanics
Type of report   : Paper (incl. supplementary materials)
Date   : 25 April 2022

Article

A system level performance analysis method for the design of a C-shape hexapod leg operating on compactive terrain

Jan van Rijn * and Hans Goosen 📧

* Correspondence: rijnvjan@gmail.com

Abstract: Remotely controlled vehicles have gained increased interest and application, like the exploration of inhospitable environments. To this end hexapods with C-shape locomotors are particularly suitable because these vehicles possess both the efficiency of wheels and the climbing capabilities of legged robots. Currently all C-legged hexapods are equipped with the same C-shape tip starting in the center of rotation, yet few to no alternative shapes that could improve the performance have been investigated. The performance is mainly characterized by three measures: traction, climbing and mobility. However, it was also found that no system level performance analysis including constraints exists. In this work a novel method is proposed to describe the system level performance of C-legged hexapods. Using this model, a computer-aided manual optimization of the leg shape is performed, from which it is observed that there is no unique optimal leg shape. The optima depend on the weight factor posed by the designer; but several leg types prove to perform better than the conventional shape. The most prominent trade-off of this hybrid shape is present between climbing and mobility, but this effect can be superseded when the shape is generated conceptually instead of analytically.

Keywords: mobile robots; C-legged hexapod; lunar rover; leg shape; traction

1. Introduction

Unmanned ground vehicles (UGVs) are valuable assets for the exploration of areas, like post-earthquakes sites or planetary surfaces, that cannot be reached by humans. For these applications legged UGVs have proven to be particularly suitable due to their ability to surmount obstacles and to traverse through irregular terrain [1]. Wheeled vehicles are energetically efficient and tracks can generate high traction, but are not suited for unstructured environments. C-shape legged vehicles (Figures 1 and 2) have a mixed advantage of both wheels and legs and only require one actuator per leg. Whereas the shape of a wheel cannot vary that much, C-shape legs can vary geometrically to a much greater extent. So one can wonder: How does the shape of a C-leg influence the performance of a hexapod?

In this work a novel method to describe this performance is presented, which describes the physical behaviour on a system level instead of through single performance metrics. The method is used to primarily assess the influence of the leg geometry on the performance, but it can also be applied to assess the impact of gait, vehicle parameters and soil parameters among others.
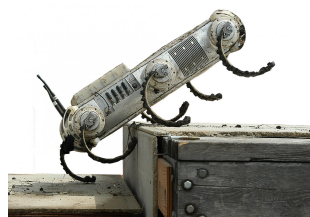

Figure 1. Rhex [2]

Figure 2. Lunar Zebro [3]

Figure 3. LZ leg [4]

The different synchronisations of the legs give rise rise to wide variety of ways of walking (gaits). The most commonly used gait is the alternating tripod. Two sets of three legs (tripods), formed by the front and rear leg at one side and the middle leg at the other side, alternatingly touch the ground. One tripod is making a rolling movement on the ground advancing the hexapod (walking period), while the other tripod is rotating freely (recovery period) to eventually engage with the ground and to take over from the other tripod. To visualize, the web page of Lunar Zebro [5] can be visited to watch a C-legged hexapod in action.

The first well-known UGV with C-legs was Rhex [6], a DARPA project; later on commercialized by Boston Dynamics to Rugged Rhex [2]. Since then multiple universities adapted this project, like KodLab's SandBot [7] and Delft University of Technology with the Zebro [8]. The prototypes have varying leg treads, but one thing they all have in common is the use of full C-shaped legs. So regarding actual applications, no other type of legs than full C-shapes are used for this kind of hexapod. Research present in literature regarding the variation of leg shapes for these hexapods is limited. Xu et al. [9] and Li et al. [10] investigated the traction of different C-shapes, but related to extreme sinkages with swimming-like behaviour using resistive force theory. Moore [11] used different leg concepts during stair climbing experiments, but focused on gait and control of each type rather than the climbing performance. Regarding mobility, Vina and Barrientos [12] described the energy analysis solely of full C-shape legs for gait and motor selection. In short, apart from the limited leg shape variation in C-type UGVs, it was observed that the performance analysis - on system level - to investigate the impact of leg shapes (or other aspects) has not yet been investigated.

In this paper, a system level performance analysis method is proposed to analytically generate and to possibly improve on the shape of the common C-shape leg. The model describes the combined physical behavior of the leg's tractive, climbing and mobility performances in a comparative manner and is used to investigate the influence of the leg geometry. A circle segment shape is used as the analytical description of this geometry for which the radius, the body height and the center of rotation offset (Figure 4) are selected as design variables. The Lunar Zebro (LZ), shown in Figure 2, is used as an example and test case to present concrete results.

The theoretical framework of the proposed model is described in Section 2 and is bounded by several aspects. Firstly, C-legged hexapods move at a relatively slow pace; to quantify, the Lunar Zebro has a nominal forward velocity of 5 cm/s (0.18 km/h). Therefore, all domains are modeled quasi-statically and dynamic effects like slip and acceleration are disregarded. This also implies that the inertia of the rotating legs is neglected. Moreover, the absolute leg mass is small (LZ: 24 g), particularly compared to the body mass (LZ: 2500 g). So the leg's mass can be assumed to be negligible. The focus of this paper is the leg performance on compactive soils, which is researched in the field of classical terramechanics (TM). In literature this theory is only available for wheels and tracks. Since the model is quasi-static, only the contact surface at the ground matters. For this reason, a C-shape leg (with a constant radius) is equal to a wheel regarding the tractive performance analysis and therefore conventional wheel models can be applied. In practice the vehicle's C-legs would have a profile like the grousers of the LZ leg (Figure 3) which increases the tractive performance. However, this contribution to the total traction can simply be superpositioned [13]. This way the profile can be disregarded and the legs are modeled with a smooth contact surface in order to keep the focus on the overall leg geometry.

Under these assumptions and boundary conditions, the traction, climbing and mobility models are implemented for a C-shape leg. The shape's impact on the separate performance metrics is investigated with a parametric analysis in Section 3. These three performance metrics describe the main functions a hexapod needs to have and are therefore included. Besides, the aforementioned literature describing performance aspects of a hexapod all

refer to one of these metrics. The design variables used are leg radius r, center of rotation (CoR) offset y_{off} and body height y_0 (Figure 4). The latter is a gait parameter describing the equilibrium position of the gait from ground to hip. Many possible sets of design variables are at hand to describe and vary the design space of a C-shape. Iterating on the knowledge of the model, these three variables were selected; the radius accounts for the contact surface and size, CoR offset for the wheel-leg ratio and body height to incorporate the gait. The sensitivity analysis of each input parameter of the model also shows the relevance of these parameters. Moreover, having too many design variables makes the analysis increasingly complex. As the planar geometry is investigated, leg width b is not. Cardile et al. [14] and Meirion-Griffith and Spenko [15] examined the influence of this parameter.

The design variables and performance objectives are conformed to a functional system level representation in order to generate optima. Constraints however bound the optima and are an important aspect of the analysis. The following three constraints are applied to the system: the rover provides a maximum available space for the legs on the chassis, the legs cannot exceed the maximum motor rpm and the hexapod is required to have a minimum forward velocity.

Utilizing the system level model and its constraints, the optimal leg shape(s) having the best performance(s) within the design space are discussed in a detailed manner in Section 4. Having utilized the LZ as test case, other cases with different conditions are analyzed. Firstly, the LZ is examined in terrestrial conditions and compared to the lunar case. This way the influence of normal weight and soil parameters is assayed. Secondly, the former case is compared to the analysis using an alternative traction model to examine the differences with the traditional traction model. Lastly practical implications, conceptual findings and design guidelines will be presented.

In this paper 'C-shape' or 'C-legged' are meant as general terms for the hybrid form of a wheel and a leg having one degree of freedom (DoF). 'Full C-shapes' are referred to as the currently used legs of RHex and LZ for example having zero to little CoR offset y_{off}.
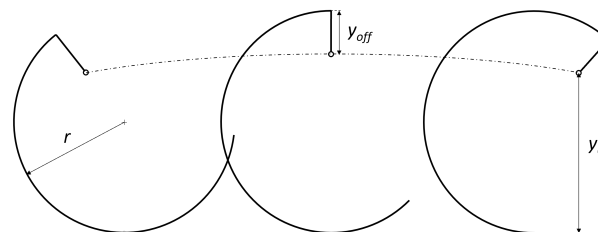

Figure 4. Leg shape description with radius r, CoR offset y_{off} and body height y_0.

2. Theory

2.1. Traction

According to [16] traction is defined as "the action of drawing or pulling something over a surface". More specifically, in the context of vehicles, it is the force exerted by a surface used to generate motion. As mentioned, terramechanical wheel models can be applied to this work, where Bekker [13] laid the groundwork of terramechanics theory by using the fundamental concepts of soil mechanics. He proposed a theory with semi-empirical relations in order to predict the performance of vehicles. Since then several researchers have expanded the theory for different applications. Worth mentioning is the work of Wong and Reece [17] improving the model by incorporating slip.

In this work, Bekker's model is used to determine the tractive performance, because of its wide availability regarding terramechanical parameters. Moreover, this model is (quasi-)static and neglects the effect of slip, in line of the assumption made in Section 1. In the first place incorporating slip would make the analysis significantly more complex, which would abate the time that could be spent on system level analysis. Secondly and more importantly, the objective of this research is to investigate the influence of the leg shape; consequently,

the analysis is of a comparative and characterizing nature instead of predictive including slip. For a part of the analysis the terramechanics model of Meirion-Griffith and Spenko [18] is used; an extension of the Bekker model, which is more accurate for wheels having a small diameter, like the Lunar Zebro. In this section the locomotor referred to is a wheel, because the theory is based on wheels. Legs however are also applicable as mentioned.

2.1.1. Equilibrium equations

To determine the forces acting on the leg, the static equilibrium is used, since the analysis is quasi-static. In Figure 5a the free body diagram of a single C-leg is shown with F the maximum soil thrust, R the soil motion resistance, N the normal force acting on a single leg, W the leg carrying weight, T the torque and DP the drawbar pull. The latter is a traction measure mostly used in the field, which is the amount of forward thrust left required for slope climbing, obstacle negotiation and acceleration. The static equilibria in both vertical and horizontal direction are simply:

$$W = N, \tag{1a}$$
$$DP = F - R. \tag{1b}$$

The free body diagram is a representation of a concentrated forces equilibrium, but the forces exerted by the soil (F, R and N) are resultants of the normal and shear stresses as shown in Figure 5b. DP is unknown and $W = m_l g$ with m_l the leg carrying mass and g the gravitational acceleration. Accordingly, the equilibrium equations are as follows:

$$W = rb \int_0^{\theta_1} \left(\underbrace{\sigma(\theta)\cos\theta + \tau(\theta)\sin\theta}_{N} \right) d\theta, \tag{2a}$$

$$DP = rb \int_0^{\theta_1} \left(\underbrace{\tau(\theta)\cos\theta}_{F} - \underbrace{\sigma(\theta)\sin\theta}_{R} \right) d\theta, \tag{2b}$$

with σ the soil normal stress, τ the shear stress of the soil, r the wheel radius, b the wheel width, θ an arbitrary angle along the wheel-soil contact and θ_1 the sinkage angle.

In practice R consists of more resistances than compaction. Bulldozing, rolling and wheel/leg flexure resistances also counteract the direction of motion. However, the magnitudes of these effects are negligible compared to the compaction, as shown by multiple researches investigating wheel-soil interaction ([14][19]). Meirion-Griffith and Spenko [15] emphasize that the bulldozing effect, the least insignificant additional resistance, actually becomes irrelevant for small and narrow wheels, like addressed in this paper.
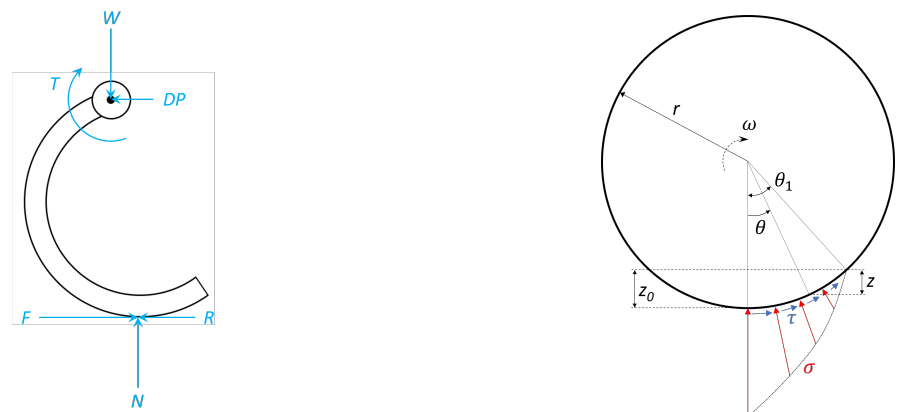
(a) Free body diagram of a C-leg   **(b)** Soil stress distributions

Figure 5. Bekker's wheel/leg–soil interaction model.

2.1.2. Soil stress distributions

The normal stress is formulated by the semi-empirical pressure-sinkage relationship, the fundamental equation in terramechanics that governs the depth a wheel sinks into the soil when subjected to a vertical load as is proposed by Bernstein and Goriatchkin [20]:

$$\sigma = kz^n, \tag{3}$$

with k the sinkage modulus, z the wheel (or leg) sinkage and n the Bernstein–Goriatchkin sinkage exponent. As the contact surface is circular it is convenient to express the sinkage in polar coordinates: $z = r(\cos\theta - \cos\theta_1)$. Bekker separated k into a cohesive sinkage modulus k_c and a frictional sinkage modulus k_ϕ, which are the most available and commonly used sinkage parameters in literature. Expressing the sinkage in polar coordinates Bekker's pressure-sinkage relationship is given as [13]:

$$\sigma(\theta) = \left(\frac{k_c}{b} + k_\phi\right)r^n(\cos\theta - \cos\theta_1)^n. \tag{4}$$

Bekker assumes the stress is constant over the width, which is why Figure 5b can be represented in 2D. It is also assumed that "the terrain reaction at all points on the contact patch is purely radial, and is equal to the normal pressure beneath a horizontal plate at the same depth in a pressure-sinkage test". The parameters k_c, k_ϕ and n are determined with such a test by performing it twofold with two plates having a different width. To prevent the effect of possible localized nonhomogeneity, the aspect ratio of such a plate has to be larger than 5 and the absolute value of b needs to be larger than 10 cm. k_c and k_ϕ can be derived by measuring the pressure at a depth of $z = 1$ for both plates, whereafter n can be determined. A more detailed description can be found in [13].

As Bekker concluded himself, his model is not accurate for wheels smaller than 50 cm. The relation is based on flat plate tests and wheels of this size do not have an approximately flat curvature anymore. Meirion-Griffith and Spenko [18] proposed an extension to Bekker's model which is also valid for small wheels, incorporating a diameter dependent term :

$$\sigma = \hat{k}z^{\hat{n}}D^{\hat{m}}, \tag{5}$$

with D the wheel diameter and $\hat{m}$ the diameter exponent, of which the value depends on the soil (negative for compactive and positive for dilative soils for example). $\hat{k}$ and $\hat{n}$ are physically similar as k and n in Equations 3 and 4, but have different dimensions, and are obtained by the same methodology described before.

The shear stress acting on the wheel-soil surface is a reaction force of the soil providing the forward thrust. In order to determine the tractive performance of a wheel without slip, the maximum shear stress the soil can bear (resulting in the maximum soil thrust F) is determined by the Mohr-Coulomb law:

$$\tau(\theta) = c + \sigma(\theta)\tan\phi, \tag{6}$$

with c the Coulombian coefficient of cohesion and ϕ the Coulombian angle of internal friction of the soil.

2.1.3. Drawbar pull

In vehicle engineering and terramechanics the drawbar pull is used to express the amount of traction. Compared to the maximum soil thrust F it also incorporates the tractive losses due to compaction. To determine the drawbar pull, the normal stress (in this case

Equation 4) and the shear stress (Equation 6) have to be substituted into the equilibrium equations of Equation 2 yielding:

$$m_l g = rb \int_0^{\theta_1} \left(kr^n (\cos\theta - \cos\theta_1)^n \cos\theta + (c + kr^n(\cos\theta - \cos\theta_1)^n \tan\phi) \sin\theta \right) d\theta, \quad (7a)$$

$$DP = rb \int_0^{\theta_1} \left((c + kr^n(\cos\theta - \cos\theta_1)^n \tan\phi) \cos\theta - kr^n(\cos\theta - \cos\theta_1)^n \sin\theta \right) d\theta. \quad (7b)$$

The vertical equilibrium (Equation 7a) is used to calculate the sinkage in the form of θ_1. Then, θ_1 is substituted into the horizontal equilibrium (Equation 7b) to determine drawbar pull DP. This way all of the parameters acting in the system are visible; using Bekker's model $k = k_c/b + k_\phi$. In summary, the tractive performance metric drawbar pull is dependent on r, b, m_l, g and soil parameters c, ϕ, k_c, k_ϕ and n.

2.2. Climbing

The ability to overcome obstacles is the principal functionality that distinguishes legged vehicles from wheeled and tracked vehicles. There are multiple ways to quantify the climbing ability of a hexapod, such as the study done by Moore [11]. But in this paper leg shape is the starting point, so it is useful to define the climbing performance by a geometric measure, which describes the obstacle height a single C-leg can surmount. The climbing behaviour in practice is quite chaotic and unpredictable due to multiple factors: Firstly the obstacle shapes and surface textures differ in any natural environment. Also, the orientation of the vehicle and its legs, the gait, with respect to the obstacle influences the climbing behaviour. Thirdly, the dynamic combination of the forward tractive force and slippage of the legs making contact with the obstacle make the climbing behaviour unpredictable. Since slip and treads are not incorporated in this work, it is assumed the normal force on the obstacle at the contact point is always sufficient.

As mentioned, in this paper a comparative research is done instead of predictive, so a more generic measure - that expresses the order of magnitude - to quantify the climbing performance is sufficient: the climbing height. This is the vertical distance measured from the ground where a C-leg can ultimately grip a right-angled corner, as shown in Figure 6. The tread is again smooth and it is assumed there is no slip at the contact point between leg and obstacle. Mathematically (Equation 8) this is the maximum height of the vertical minimum, where the active tripod is positioned upright and the passive (gripping) tripod is pointed upwards (rotation angle = π), as shown in Figure 6. Naturally, the leg sinkage decreases the climbing height and is extracted.

$$y_c = r_e + y' - z_0, \quad (8a)$$

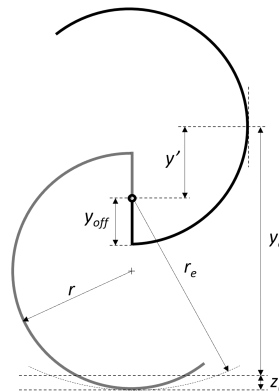$$y_c = 3r - 2y_{\text{off}} - z_0, \quad (8b)$$

Figure 6. Schematic of the climbing height metric.

with y_c the climbing height, y' the gripping point, z_0 the total sinkage and r_e the effective leg radius equal to $2r - y_{\text{off}}$. For a general shape, the latter can be determined by calculating the vertical coordinate where the first derivative over y is equal to zero. Equation 8a is a general definition whereas Equation 8b describes the climbing height for the shape description used in this paper.

2.3. Mobility

The mobility of a hexapod describes how efficiently the vehicle moves. Vina and Barrientos [12] investigated this for a C-leg and used a well suited metric: the distance covered per consumed Joule. This way not only the energy cost of one cycle is accounted for, but also the distance the hexapod has advanced. Besides, it allows to compare robots of different sizes and weights. In order to determine this mobility metric, firstly the kinematics of a rolling C-leg are discussed and secondly the energy equations.

Whereas for the traction analysis sinkage is taken into account, for the kinematic analysis it is not incorporated. Due to the constant contact radius the sinkage is constant implying no influence on the performance regarding mobility. Because of the quasi-static approach the changes in velocity, and thus the kinetic energy, are negligible comparing it to the potential energy. Modeling with compactive soils, the energy dissipated by compaction is found to be significant. This factor is therefore incorporated within the model in contrast to the model of Vina and Barrientos. As already mentioned in Section 2.1.1, additional resistances are assumed to be negligible.

2.3.1. Kinematics

To describe the motion of a C-leg in a 2D plane first a starting position and a frame of reference needs to be set. The starting position is at the upright instance of the leg in the recovery period with the origin located at the leg's CoR (e.g. hip) as shown in Figure 7. The coordinates of any point on the starting leg is described by Equation 9:

$$\vec{P}_i = \begin{bmatrix} x_i \\ y_i \end{bmatrix} = \begin{bmatrix} r \sin \alpha \\ -r \cos \alpha + y_s \end{bmatrix}, \tag{9}$$

with $\vec{P}_0$ the position of a point on the leg in the starting configuration, x_i the initial x-coordinate, y_i the initial y-coordinate, α the leg angle and y_s the distance between CoR and the circular center equal to $r - y_{\text{off}}$.
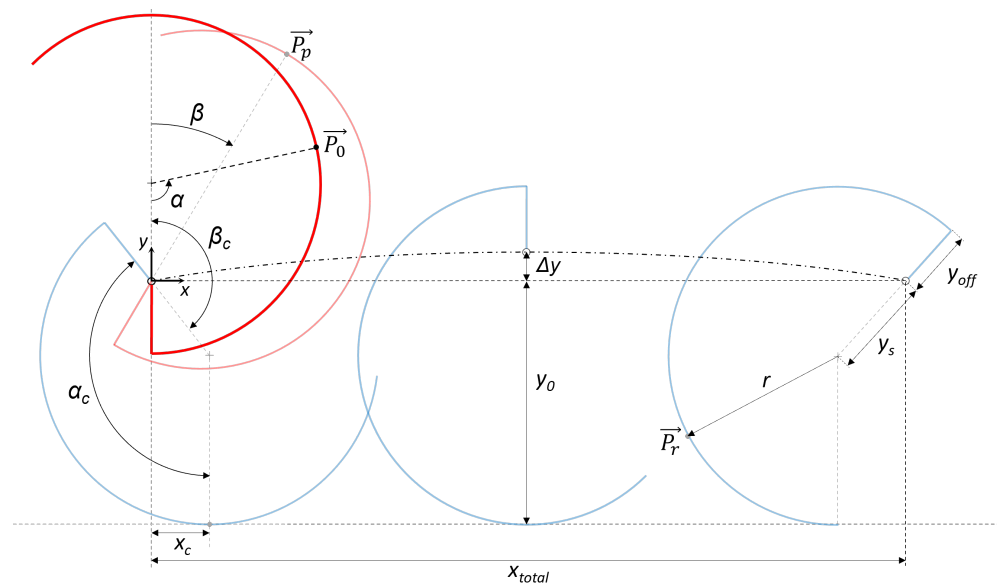

Figure 7. Schematic of the kinematic properties of a C-leg; horizontally stretched for illustrative purposes. The red and blue instances are during the recovery and walking period, respectively.

During recovery the leg is pivoting around the CoR until it touches the ground, so a transformation by a clockwise rotation matrix is performed:

$$\vec{P}_p = \begin{bmatrix} x \\ y \end{bmatrix} = \begin{bmatrix} \cos(\beta) & \sin(\beta) \\ -\sin(\beta) & \cos(\beta) \end{bmatrix} \begin{bmatrix} x_i \\ y_i \end{bmatrix}, \qquad \text{for } 0 \leq \beta < \beta_c, \tag{10}$$

with $\vec{P}_p$ the position of a point on the leg in the recovery period, x the x-coordinate, y the initial y-coordinate, β the rotation angle and β_c the ground contact angle.

The latter forms the boundary where the described pivoting motion of the recovery period turns into rolling motion of the walking period. It is calculated by determining the rotation angle at which the lowest point of the leg is equal to body height y_0, which is the gait's equilibrium position (Figure 7). First, the lowest points of the different rotated leg instances are determined by calculating the leg angle of the minimum of y. The written out equation of y (from Equation 10) and its extreme values are as follows:

$$y = -r(\sin \alpha \sin \beta + \cos \alpha \cos \beta) + y_s \cos \beta, \qquad \text{for } 0 \leq \beta < \beta_c, \tag{11a}$$

$$\frac{dy}{d\alpha} = r(\cos \beta \sin \alpha - \sin \beta \cos \alpha) = r \sin(\alpha - \beta) = 0, \qquad \text{for } 0 \leq \beta < \beta_c. \tag{11b}$$

The solutions of Equation 11b, denoted by $\alpha_{\min}$, are then:

$$\alpha_{\min} - \beta = n\pi, \qquad n = 0, 1 \quad \text{and for } 0 \leq \beta < \beta_c, \tag{12}$$

with $\alpha_{\min}$ the vertical minimum leg angle. Due to the way α is constructed, the solution for the minimum and maximum always corresponds with $n = 0$ and $n = 1$, respectively. Conveniently, this means that the leg angle is equal to the rotation angle at the ground contact point: $\alpha_{\min} = \beta$.

In the gait's equilibrium position, the lowest point of the trajectory, the axle is a distance y_0 from the ground ($y = 0$). The rotation angle where the leg comes in contact with the ground first, touch angle β_c, must be determined. This is the boundary between pivoting and rolling motion (traction becomes present), the cycle starting point for forward motion. This boundary is at $y = 0$ with α being a ground contact angle. So setting Eq. 11a equal to zero, substituting $r - y_{\text{off}}$ for y_s and β for α (Equation 12) yields:

$$-r(\sin^2 \beta_c + \cos^2 \beta_c) + (r - y_{\text{off}}) \cos \beta_c = -y_0, \tag{13a}$$

$$\beta_c = \cos^{-1}\left(\frac{r - y_0}{r - y_{\text{off}}}\right). \tag{13b}$$

Equation 13b can also be derived graphically from Figure 7.

For rotation angles larger than the ground contact angle the motion type changes form pivoting to rolling, which will make the hexapod move. So horizontal and vertical translations must be applied to the kinematic description of $\vec{P}_p$ to account for this:

$$\vec{P}_r = \begin{bmatrix} x \\ y \end{bmatrix} + \begin{bmatrix} x_t + s \\ y_t \end{bmatrix}, \qquad \text{for } \beta_c \leq \beta < 2\pi - \beta_c, \tag{14}$$

with x_t and y_t the horizontal and vertical rolling translations respectively and s the arc length over which the leg has rolled. The rolling translations serve as corrections, since the leg has to be moved from the pivoted position to the forwardly advanced position. For both directions this is the distance between the ground contact instance and the lowest point of the current leg instance ($\alpha = \alpha_{\min}$):

$$x_t = x_c - x|_{\alpha = \alpha_{\min}}, \qquad \text{for } \beta_c \leq \beta < 2\pi - \beta_c, \tag{15a}$$

$$y_t = y_0 - y|_{\alpha = \alpha_{\min}}, \qquad \text{for } \beta_c \leq \beta < 2\pi - \beta, \tag{15b}$$

with x_c the x-coordinate of the ground contact instance as shown in Figure 7. In this case a circle leg shape is used, so the the arc length is calculated as follows:

$$s = r(\alpha_{\min} - \alpha_c), \qquad \text{for } \beta_c \leq \beta < 2\pi - \beta_c, \tag{16}$$

with α_c the ground contact leg angle as shown in Figure 7.

The total, written out kinematic equation over one cycle for a C-shape leg with a CoR offset is as follows:

$$\vec{P}_p = \begin{bmatrix} \cos(\beta) & \sin(\beta) \\ -\sin(\beta) & \cos(\beta) \end{bmatrix} \begin{bmatrix} r\sin\alpha \\ -r\cos\alpha + y_s \end{bmatrix}, \qquad \text{for } 0 \leq \beta < \beta_c, \tag{17a}$$

$$\vec{P}_r = \begin{bmatrix} \cos(\beta) & \sin(\beta) \\ -\sin(\beta) & \cos(\beta) \end{bmatrix} \begin{bmatrix} r\sin\alpha \\ -r\cos\alpha + y_s \end{bmatrix} + \begin{bmatrix} x_c - x|_{\alpha=\alpha_{\min}} + r(\alpha_{\min} - \alpha_c) \\ y_0 - y|_{\alpha=\alpha_{\min}} \end{bmatrix}, \tag{17b}$$

$$\text{for } \beta_c \leq \beta < 2\pi - \beta_c. \tag{17c}$$

2.3.2. Consumed energy

The energy that the hexapod needs to consume to move itself is determined by the gravitational and compaction resistances. While walking, the vehicle moves up- and downwards resulting in a potential per cycle, gravitational energy. As the leg carrying weight is attached to the hip, it is described as follows:

$$E_g = m_l g \Delta y, \tag{18}$$

with E_g the consumed gravitational energy per cycle and Δy the hip height variation. The latter is determined by $\Delta y = 2r - y_{\text{off}} - y_0$ (Figure 7).

The hexapod is also resisted by the compaction of the soil:

$$E_r = R x_{\text{total}}, \tag{19}$$

with E_r the consumed compaction energy per cycle and x_{total} the distance covered per cycle. Compaction R can be calculated with Equation 2b. Using Figure 7 x_{total} is calculated by:

$$x_{\text{total}} = 2(x_c + r(\pi - \beta_c)). \tag{20}$$

2.3.3. Distance covered per consumed Joule

As mentioned, the horizontal distance the hexapod advances consuming one Joule is employed as the mobility performance metric. Applying the kinematics and energy equations, the distance covered per Joule η_x is as follows:

$$\eta_x = \frac{x_{\text{total}}}{E_g + E_r}. \tag{21}$$

3. Parametric analysis

The aim of this section is to investigate the influence of every parameter in order to set up the system level analysis. The physical behaviour of every performance metric is mapped with an emphasis on the influence of the design variables as shown in Figure 4). Table 1 specifies the logarithmic sensitivities.

3.1. Traction

Geometrically the drawbar pull is dependent on the contact area (Equation 7b); the interface between soil and leg. The radius of curvature and width make up the outer surface of the leg, where the contact area is determined by the sinkage, which is in turn dependent on the leg carrying load. So only the leg radius has an impact, regarding the three design variables, having an exponentially growing relationship with the drawbar pull (Figure 8); though in a rather insignificant degree (Table 1).

Table 1. Dependency and logarithmic sensitivity of the performance metrics on input parameters. With drawbar pull DP, climbing height y_c and distance covered per consumed Joule η_x. The constant values and ranges used can be found in Table A1.

Symbol	Description	DP	y_c	η_x
r	Leg radius (m)	0.1 - 0.4	1	-0.15
y_{off}	Vertical CoR offset from leg tip (m)	n/a	0 - -2	0 - 1
y_0	CoR height from ground (m)	n/a	n/a	0.1 - 1
b	Leg width (m)	0.2	0	0.15
c	Coulombian coefficient of cohesion (Pa)	0.2 - 0.6	n/a	n/a
ϕ	Coulombian angle of internal friction (°)	1	n/a	n/a
n	Bernstein–Goriatchkin sinkage exponent (-)	1.4	0	2
k_c	Bekker cohesive sinkage modulus (Pa/m^{n-1})	0	0	0
k_ϕ	Bekker frictional sinkage modulus (Pa/m^n)	0	0	0
m_l	Leg carrying mass (kg)	0.8	0	-1.25
g	Gravitational acceleration (m/s^2)	0.8	0	-1.25

Other parameters that have a significant impact on the magnitude of the drawbar pull are the angle of internal friction and the sinkage exponent (soil type), and the vehicle mass and gravitational acceleration (normal weight).

3.2. Climbing height

Equation 8b and Figure 9 shows that the radius and the CoR offset have a positive and negative linear impact on the climbing height, respectively. A higher radius increases gripping point y' whereas it decreases for higher CoR offsets. Both design variables have significant sensitivities within the ranges (Table 1). The body height y_0 does not impact climbing because the standing legs are in upright position r_e during this operation (Figure 6). Sinkage component z_0 has a minor contribution to the climbing height resulting in low sensitivities of its (mainly geophysical) parameters.
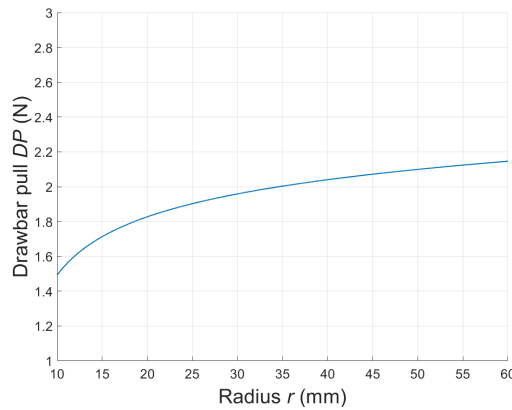

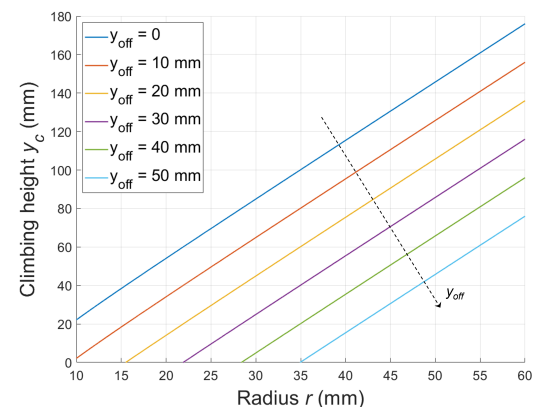**Figure 8.** Drawbar pull DP as a function of leg radius r. $y_{off} = 0$, $y_0 = 50\,mm$.

Figure 9. Climbing height y_c as a function of leg radius r. Variable y_{off}, $y_0 = 50\,mm$.

3.3. Mobility

The mobility metric is influenced by all three design variables as shown in Figure 10. As shown in these graphs, the behavior is bounded by an asymptote signifying the geometry from where the leg has no contact with the ground; i.e. when effective radius r_e is smaller than body height y_0. Evidently, losing contact with the ground is a modelling effect. Nonetheless this represents the gait requirement of a hexapod to have a certain height at which it operates nominally (body height y_0). So smaller effective radii increase the mobility up to the body height. Considering Equation 21, x_{total} decreases because the ground contact length decreases. The consumed energy also decreases because hip height

variation decreases for smaller radii. However, the consumed energy decreases to a larger degree than the distance covered, yielding the exponentially decaying behavior.

Thus the performance regarding mobility increases for a decreasing effective radius $(2r - y_{\text{off}})$ up to the ground contact limit. As indicated by Figure 10b the body height has a positive effect on mobility. So in this manner a hexapod walking with a higher gait covers a larger distance consuming one Joule. Other parameters that have a significant impact on the magnitude of η_x are the vehicle mass and gravitational acceleration (normal weight), and the sinkage exponent (soil type).
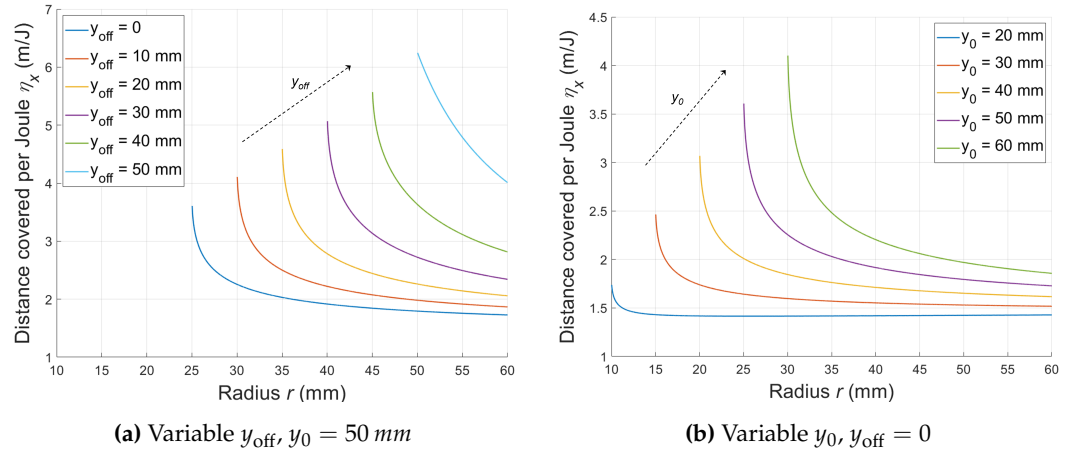

(a) Variable y_{off}, $y_0 = 50\,mm$ **(b)** Variable y_0, $y_{\text{off}} = 0$

Figure 10. Distance covered per consumed Joule η_x as a function of leg radius r.

4. System level analysis

The goal of this research is to generate leg shapes with a system level based performance analysis. An exemplary test case, the Lunar Zebro, is used to show tangible results. Its characteristics fit well in the scope of this work. This hexapod, also equipped with classical full C-legs, is developed to operate on lunar soil, compactive terrain. The LZ in the lunar environment is the main case examined, with Bekker's pressure-sinkage relationship being used for the terramechanics model.

First the model parameters of the main case together with relevant background are provided. Next, whereas in Section 3 the performance metrics are separately discussed, they must be combined to one system level analysis. Three design variables and objectives are present, so this must be reduced to a lower order to enable the representation of results. These results are leg shape optima, which become apparent when incorporating the constraints that act on the system and bound the design space; subsequently determining the feasible domain of possible leg shapes. The constraints are explained, how they interact and how to modify them to augment the feasible region in order to yield better results. Then, most of all, the different shape outcomes are discussed and compared. Having varied only the design variables, two variations on the main case are discussed. Firstly the LZ under terrestrial conditions is analyzed and compared to the main case. Secondly, the small-diameter terramechanics model is used and compared to the terrestrial case, where Bekker's model is used. Lastly guidelines for the design of a hexapod leg are presented.

4.1. Lunar Zebro model parameters

This planetary nano rover is developed to operate on the lunar surface. Operating on the Moon, the most significant difference is the gravitational acceleration being a factor 6 less. Besides, almost the entire surface of the Moon is covered with a layer of unconsolidated solid rock, called lunar regolith. The top layer, the surface the lunar rover interacts with, is the finely sized fraction of regolith referred to as lunar soil and resembles dry loose sand. The corresponding geophysical parameters and the rest of the LZ parameter values are given by Table 2.

Table 2. Input parameters of the main case. Vehicle constants are LZ based exemplary values, environmental constants[1] are retrieved from [21].

Symbol	Description	Value
b	Leg width (mm)	20
c	Coulombian coefficient of cohesion (kPa)	0.52[1]
ϕ	Coulombian angle of internal friction (°)	42[1]
n	Bernstein–Goriatchkin sinkage exponent (-)	1[1]
k_c	Bekker cohesive sinkage modulus (kPa/m^{n-1})	1.4[1]
k_ϕ	Bekker frictional sinkage modulus (kPa/m^n)	820[1]
m	Vehicle mass (kg)	2.5
g	Gravitational acceleration (m/s^2)	1.635[1]
r_0	Maximum available space (mm)	60
$v_{\min}$	Minimum nominal velocity (cm/s)	4.5
ω_w	Angular leg speed during walking step (rad/s)	1
ω_m	Maximum angular motor speed (rad/s)	1280
i	Gearbox transmission ratio gearbox (-)	256

The vehicle's weight distribution over the legs is not constant due to the alternating gait and it varies when the body walks on slopes, climbs or steers. These effects have a small impact though and are not incorporated. Moreover, the nominal operating characteristics of a hexapod are investigated. Nonetheless the normal weight distribution in this static state needs to be accounted for. Seeing that three legs carry the vehicle weight, the middle leg at one side carries half whereas the front and rear legs both carry a quarter of the weight.

For the performance analysis of traction, the leg carrying mass m_l of the middle leg is used ($\frac{m}{2}$) and substituted in Equation 7. The normal weight has a negative impact on the drawbar pull, which implies that the DP of the middle leg is lower than the front and rear legs' DP on the other side. So the middle leg is the bottleneck for the tractive performance. As to climbing, the middle leg's carrying mass is also used because the gripping leg is on this side of the hexapod. For the performance analysis of the mobility, the average leg carrying mass $m_l = \frac{m}{3}$ is applied and substituted in Equation 18. The average is used because the consumed energy is cumulative over all legs.

4.2. Representation

When performing multi-variable analyses the graphical representation is always a challenge. Three design variables (r, y_{off} and y_0) and three objectives (DP, y_c and η_x) are investigated in this paper. Nonetheless a representation capturing the system level behavior is developed with a three-dimensional contour plot shown in Figure 11. The performance metrics of mobility (distance covered per Joule η_x) and climbing (climbing height y_c) are plotted as a function of the leg radius r and CoR offset y_{off}. Both functions are limited by the asymptote described in Section 3.3 signifying the point where the leg loses contact with the ground. η_x increases to the top left corner whereas y_c increases to the bottom right corner. This is the most prominent trade-off and will be elaborated later. For representation purposes the isolines of y_c are assumed to have a linear sensitivity, since the sinkage variation is negligible (<1% within the feasible region). Body height y_0 is held constant and tractive performance metric DP (drawbar pull) is depicted on the upper x-axis.

This representation can be composed due to the fact that reductions can be made. With the knowledge of the parametric analysis performed in Section 3 the following three observations substantiate this: traction is only dependent on the leg radius, climbing is not dependent on body height and mobility is impacted by all three design variables.

First and foremost, since it only influences the mobility, body height y_0 is therefore not incorporated as design variable and is kept constant. In addition, this parameter is of a gait nature and does not describe the leg shape. In Section 3.3 it is demonstrated that increasing y_0 increases the overall performance (since y_0 does not impact DP and y_c). However, y_0 is
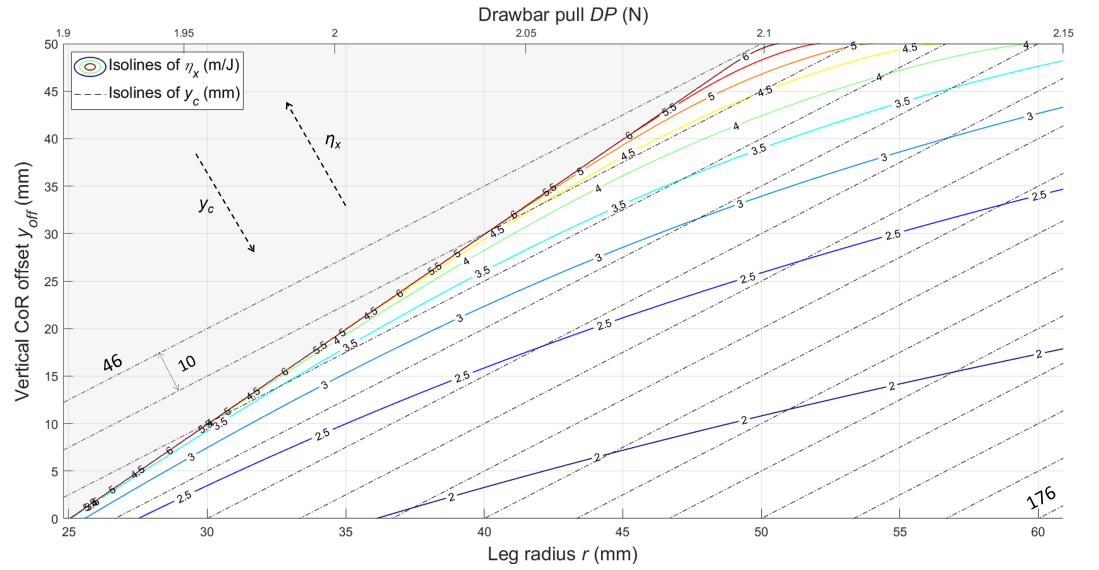
Figure 11. System level representation with radius r and CoR offset y_{off} as design variables (body height $y_0 = 50$ *mm*); distance covered per Joule η_x and climbing height y_c as objective functions (drawbar pull DP can be read on upper x-axis). y_c isolines are assumed to have a linear sensitivity.

bounded by toppling resulting in a limit of 50 mm (LZ based). In figure A1 of the appendix the impact of the body height is shown for a multi-variable analysis.

It is also not necessary to represent traction as objective function since it only depends on the radius. Therefore, the drawbar pull can be depicted on the same axis as the radius. DP also has a low sensitivity (Section 3) making it less relevant than the other two metrics.

In summary, Figure 11 can be used to determine the values of the three performance metrics for the full design space. To represent the design optima however, this design space is reduced to a feasible region by constraints, which will be elaborated in Section 4.3. As to the representation of these design optima, the climbing height is used as a set design requirement - instead of function values by means of isolines - to maintain the overview.

4.3. Constraints

The leg design options are limited by the principle that the legs need to make contact with the soil at the predetermined body height y_0. In other words: the effective radius has a minimum. This constraint is discussed in Section 3.3 and referred to as the asymptote. This is also visible by the η_x isolines of Figure 11 and described as follows:

$$2r - y_{\text{off}} \geq y_0. \tag{22}$$

The rover provides a maximum available space r_0 for the legs on the chassis. The front and rear legs' size is limited by the relative position of the middle leg axle:

$$2r - y_{\text{off}} \leq r_0. \tag{23}$$

The hexapod is required to have a minimum forward velocity $v_{\min}$. Firstly, $v_{\min}$ is dependent on the distance covered per walking step x_{total}. Besides, it depends on the length of contact with the ground, which takes a certain time posed by the angular velocity:

$$t_w = \frac{\beta_w}{\omega_w} = \frac{2(\pi - \beta_c)}{\omega_w}, \tag{24}$$

with t_w the walking time, β_w the walking angle (from soil entry to exit), ω_w the angular leg speed during a walking step, β_c the soil entry angle as can be retrieved by Equation 13b.

Subsequently the minimum nominal walking speed $v_{\min}$ is as follows:

$$\frac{x_{\text{total}}}{t_w} \geq v_{\min}. \tag{25}$$

The legs cannot exceed the maximum motor rpm. The angular velocity of the leg during the walking period is set, which is 1 rad/s for the Lunar Zebro. However, when a leg is in the recovery period, it needs a certain angular speed to be 'back in time' again for the next step. Consequently, when the recovery angle is too large or the recovery time too small, the maximum rpm the motor can handle is exceeded. In other words, the angular velocity during recovery is constrained.

The walking time is equal to the recovery time, thus the recovery angle ($\beta_r = 2\pi - \beta_w$) needs to be covered in the same time as the walking angle is covered at walking speed ω_w:

$$\left(\frac{2\pi}{\beta_w} - 1\right)\omega_w \leq \frac{\omega_m}{i}, \tag{26}$$

with ω_m the maximum angular motor speed and i the transmission ratio from motor to leg.

Above constraints concern limits on the rpms of the motor. As to the motor torque, the transmission provides sufficient torque so that its maximum is not exceeded during nominal operation.

These constraints jointly limit the design space and form a feasible region as shown in Figure 12. The minimal contact constraint is not visible because it simply equals the asymptote and minimum nominal velocity constraint is inactive at the value of this test case (Table 2). The climbing height is depicted here as a design requirement with a certain value, as mentioned in Section 4.2. As a result the general feasible region lies between the motor and space constraint, because the climbing height line is movable.

In the example of Figure 12 this line is approximately parallel with the isoline η_x, which means any point on the climbing height line (within the feasible region) yields about the same performance regarding mobility. However, the traction optimum lies in the right corner since the drawbar pull increases for larger leg radii (upper x-axis). In the following section the possible leg shape types resulting from the performance analysis are explained.
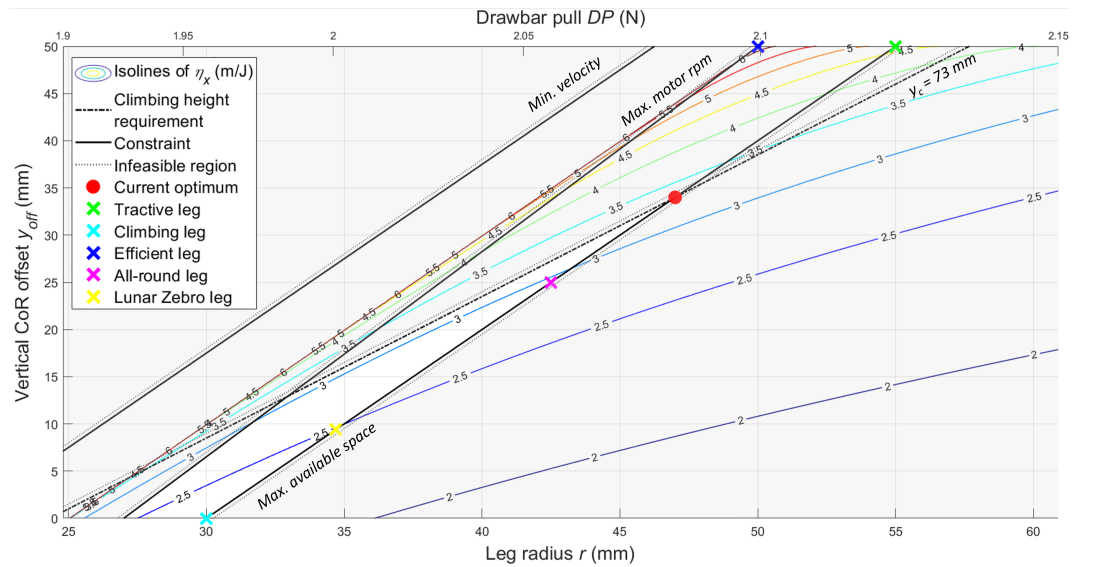

Figure 12. System level representation including constraints and design points. With radius r and CoR offset y_{off} as design variables (body height $y_0 = 50$ *mm*); and distance covered per Joule η_x as objective function. Climbing height y_c functions as design requirement, drawbar pull DP can be read on the upper x-axis. The non-shaded area is the feasible region.

4.4. Leg shape outcomes: main case

There is no unique optimum. Due to the trade-offs there are multiple design points which depend on the preference of the designer. In Figure 12 the three optima for each performance metric are shown by markers, together with the design points for a possible all-round leg and the current leg design of the Lunar Zebro.

The actual shapes of these different leg types is shown in Figure 13 together with the quantification of the performance. As this research is comparative, the performance is quantified by a relative metric. Every performance outcome is related to the feasible maximum, resulting in a ratio. For example, the distance covered per Joule η_x of the tractive leg is 4.79 m/J. The maximum of η_x within in the feasible region is equal to 6.15 m/J (the efficient leg). Accordingly, the relative performance regarding mobility is 77,8% for the tractive leg (and 100% for the efficient leg). To quantify and compare the performance on system level, the average per leg type is presented by the red bars.

As to the shape outcomes, firstly, the leg with optimal traction has the largest possible leg radius providing maximal contact area between leg and soil, as expected. The outcome of the climbing leg has zero CoR offset and a maximized radius within the available space resulting in a high gripping point. Lastly, the efficient leg's CoR offset and radius are equal to the body height leading to a zero hip height variation. Consequently, no potential energy needs to be consumed and only the compaction consumption must be accounted for. The all-round leg is a compromise regarding leg geometry and the current Lunar Zebro leg tends to be a climbing leg. Recapitulating, a tractive leg has a high contact surface, a climbing leg has a full C-shape and an efficient leg is identical with a wheel.

As to the relative performances, the trade-off between climbing and mobility that has been described is clearly visible seeing that the climbing leg has poor mobility and the efficient leg does not perform well with regard to climbing. Besides, the high sensitivity (particularly at the asymptote) of the mobility metric is visible by the significant differences in the bar chart with the climbing leg having a mobility performance ratio of 36.2%. Additionally, the all-round leg has an intermediate shape, but the mobility is relatively low. On the contrary, the low traction sensitivity described in Section 3.1 is apparent as the leg with the lowest traction still is 92.2% of the feasible maximum.

On system level, regarding average performances, the differences between different leg types are not significant. The tractive and efficient leg perform best, particularly due to the high sensitivity of the mobility. Figure 14 shows a complete overview of the overall performance within the feasible region, rather than merely the five shape types. The average performance is higher at high CoR offsets; again due to the high sensitivity of η_x.
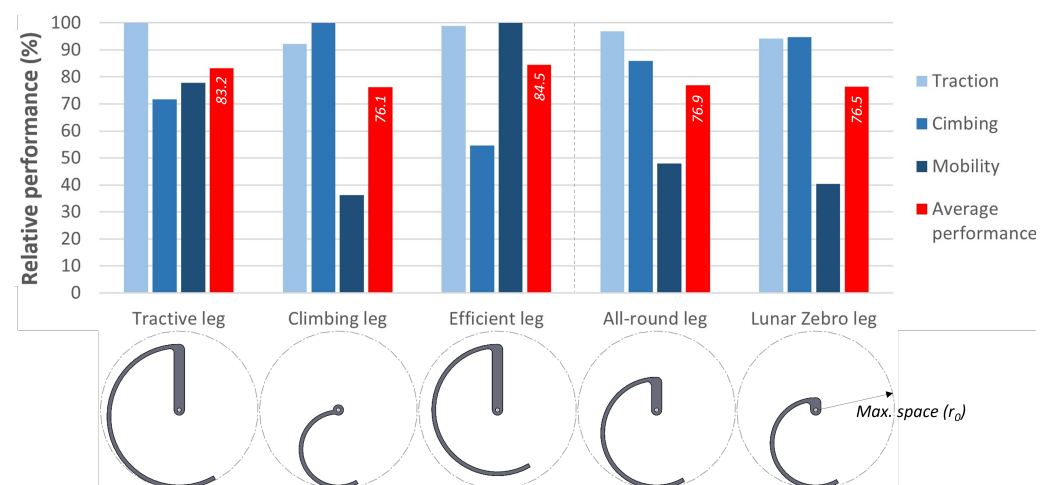

Figure 13. Performance of different leg types (optima and design points) of the main case, represented as the percentage of the feasible maximum for each of the three metrics ($DP = 2.12$ N, $y_c = 84.9$ mm, $\eta_x = 6.15$ m/J) together with their average.
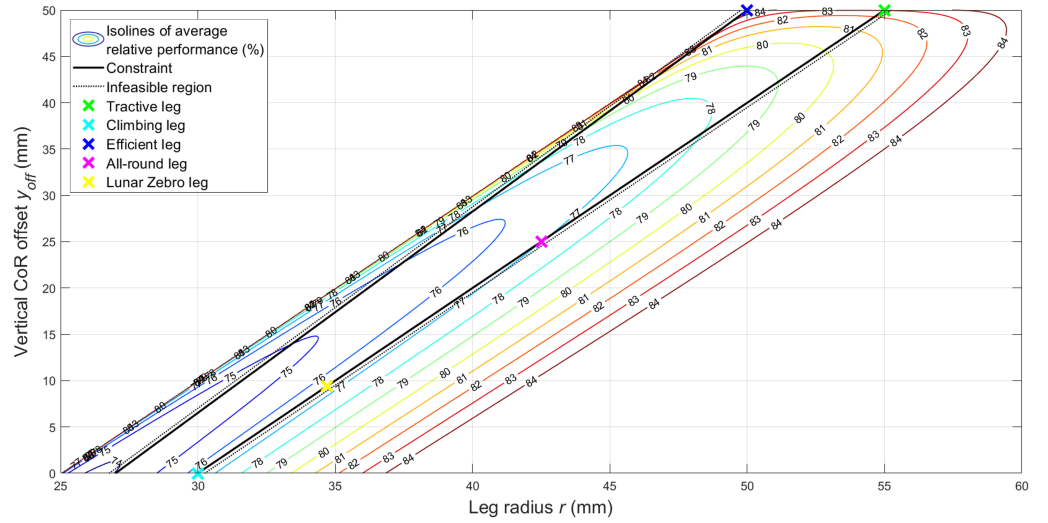
Figure 14. Average relative performance in feasible region as a function of design variables radius r and CoR offset y_{off} (body height $y_0 = 50\ mm$), bounded by max. rpm (left) and max. available space (right) constraints. Design points are indicated by the markers again.

4.5. Variations

More variables act on the system than the proposed design variables. All input parameters are listed in Table 1, in which it is shown other parameters than the design variables have a significant sensitivity. Based on that, two alternative cases are described to both evaluate the system level performance analysis further and to observe the design impact.

Firstly, a case with the same vehicle parameters - but in terrestrial conditions - is discussed and compared with the results of Section 4.4. Secondly, a similar analysis, but using the Meirion-Griffith and Spenko terramechanics model, is performed and compared to the terrestrial case (Bekker's model). The ground for doing so is the fact that the lunar soil pressure-sinkage properties of this model are not available in literature and only flat plate tests are performed on soils existing on Earth. The absolute values of each performance metric's maximum within the feasible region are stated in Table 3.

Table 3. Absolute values of feasible maximum performances per case.

Case	DP (N)	y_c (mm)	η_x (m/J)
Main case: lunar conditions	2.12	84.9	6.15
Terrestrial conditions	7.61	73.4	0.502
Small-diameter TM model (terrestrial)	6.90	76.9	0.670

4.5.1. Terrestrial conditions

In the previous section the system level performance analysis is illustrated with the test case of the Lunar Zebro, a hexapod operating in lunar conditions. It is interesting to evaluate how the performance would be under different conditions like on earth and to compare this. The newly investigated soil is loose sand with geophysical properties [22] $c = 1.00\ kPa$, $\phi = 30°$, $n = 1.1$, $k_c = 0.90\ kPa/m^{n-1}$ and $k_\phi = 1523\ kPa/m^n$ and with the terrestrial gravitational acceleration $g = 9.81\ m/s^2$. This way sensitive geophysical parameters c, ϕ and n and the normal weight W with a varied g is accounted for.

Figure 15 shows again the performance ratio within the feasible region, which is identical to the lunar case since the constraints are not affected by the change of environment. This means that the outcomes of the different leg shape types are also equal. Nevertheless, the magnitude of the performances are different than the Zebro operating on the Moon. Looking at Table 3 the traction is a factor 3.5 higher due to the increased normal weight resulting in a higher maximum soil thrust. It must be noted that, using the drawbar pull for traversing slopes, the load case is also increased to due the increased gravity. The
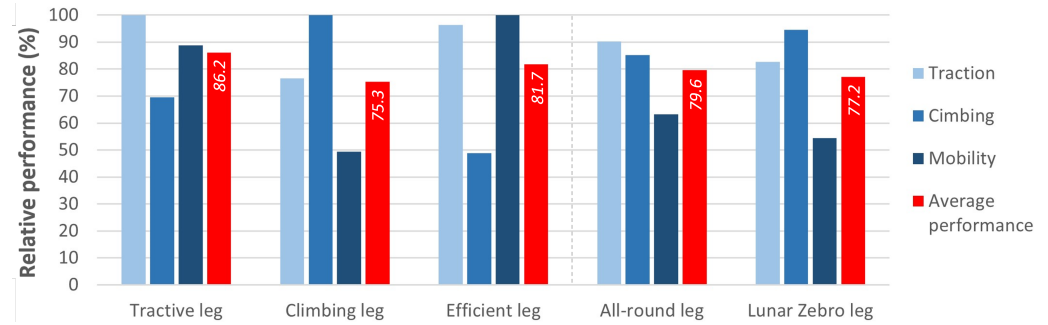
Figure 15. Performance of different leg types (optima and design points) of the terrestrial case, represented as the percentage of the feasible maximum for each of the three metrics ($DP = 7.61 \ N, y_c = 73.4 \ mm, \eta_x = 0.502 \ m/J$) together with their average.

mobility on Earth is significantly worse with a decrease of the maximum distance covered per Joule of factor 12.3. Firstly this is due to the increase of the potential energy caused by the increased gravitational acceleration, which - secondly - leads to an increased normal weight, thus increased sinkage, thus an increase of the compaction energy. So whereas the distance covered is equal since the leg shape has not changed, the consumed energy has increased significantly. The climbing height is slightly lower with a factor 1.15 owing to the increased sinkage, whilst the gripping height is equal.

Summarily, the relative performance shows about the same outcomes (Figure 15), while the absolute performance is significantly different on Earth. Looking at the averages, the performance ratio is generally a little better on Earth. Besides, it is worth noting that the terrestrial tractive leg performs best now and that the all-round leg improves relatively more compared to the lunar case. So the averages are not really affected by the change of environment, but on the other hand the separate metrics are affected notably. The traction's sensitivity is larger under terrestrial conditions resulting in lower ratios. The sensitivity of the mobility, however, is lower such that the ratios of this metric improve.

4.5.2. Small-diameter terramechanics model

As described in Section 1 the pressure-sinkage relationship is not (yet) described by one exact analytical equation. There are various semi-empirical equations describing this phenomenon. For the main analysis (Section 4.4) the fundamental Bekker equation [13] is used to calculate the drawbar pull, compaction and sinkage due to the availability of lunar soil parameters. However, as explained, the accuracy of this model worsens at diameters smaller than 50 cm used in this test case and the pressure-sinkage relationship of Meirion-Griffith and Spenko (Equation 5) should be used. Though this is less of an issue for the comparative nature of the analysis.

Nonetheless it is interesting to see the difference in outcomes between the two models on a system level. So the same analysis as Section 4.5.1 with terrestrial loose sand is performed and compared to it, but using Equation 5 instead of Equation 4 with diameter dependent pressure-sinkage parameters $\hat{k} = 1604 \ kPa/m^n$, $\hat{n} = 0.8$ and $\hat{m} = 0.8$ [18].

Looking at Table 3 the maximum performances per metric (within the feasible region) do not show the significant differences described between Moon and Earth, which are all due to the decreased sinkage of the small-diameter model. It leads to a reduced contact surface, thus a reduced traction (9.4%). As to climbing, the smaller sinkage increases the climbing height (4.8%). The mobility increases - more significantly - by 33% since the smaller sinkage reduces the consumed compaction energy.

Considering the relative performances depicted by Figure 16, the averages are practically equal to the performances determined with the Bekker model. As to the separate metrics, also here the mobility only shows a noteworthy difference. Reasonably, the mobility's sensitivity also increases using the small-diameter model.
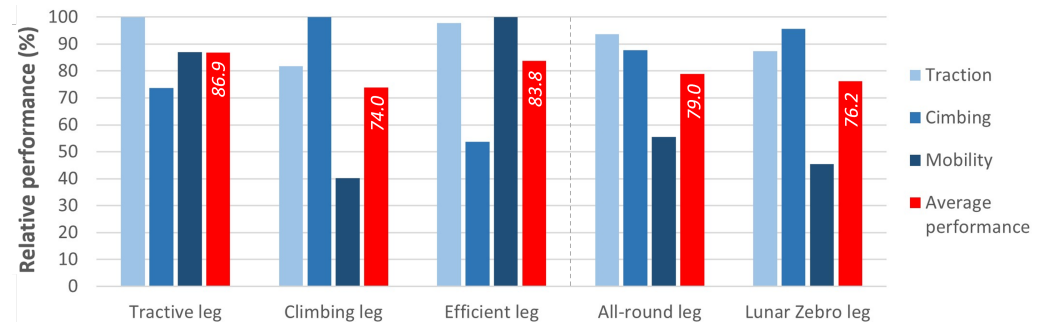
Figure 16. Performance of different leg types (optima and design points) of the small-diameter TM model case, represented as the percentage of the feasible maximum for each of the three metrics ($DP = 6.90\ N$, $y_c = 76.9\ mm$, $\eta_x = 0.670\ m/J$) together with their average.

4.6. Design guidelines

4.6.1. Constraint analysis

In the previous sections the results of the system level performance analysis are discussed. Performances vary, but the feasible region remains unchanged; so do the optima (leg shape types). Enlarging the feasible region can be done by expanding the constraints. Although the Lunar Zebro has these constraints for a reason, in a general sense it is valuable to examine how to increase the optimal performance even more.

Remarkably, almost all optimal shapes are located on the line of the maximum available space (Figure 12). In other words, larger legs increase the performance generally, thus the space between the axles should be maximized. Besides, a higher body height results in an increased performance with respect to the mobility (Section 3.3, Figure A1). However, this will also increase the size of the rover body leading to a higher weight, which is unfavourable for mobility and climbing. Also, for operation purposes the hexapod may need to be small in size. The Lunar Zebro for example must have minimal weight (and size) since it is sent into space and every gram counts financially in these ventures.

A notable side benefit of using the maximum available space for the leg is the increased nominal vehicle velocity. In Figure 12 it is depicted by a certain constraint value, but it increases by moving it to the parallel axle space constraint. In this example the required nominal velocity of 4.5 cm/s is always met due to the inactivity of the constraint at this value. But the nominal velocity of legs using the maximum available space is 5.65 cm/s whereas the efficient leg (left boundary of the feasible region) moves at 5 cm/s. So in this example the large legs are 13% faster than the efficient leg, which emphasizes the advantage again of larger legs.

4.6.2. Conceptual approach

As mentioned the most prominent trade-off is the one between climbing and mobility, causing a compromise for the average performance. However, this is the case within the mathematical shape description used in previous analyses. Regarding the design optimization conceptually, the outcome could be different and/or better. This can be done by studying the fundamental basis of Section 3, where the optimal shape for every performance metric is separately described. The climbing height is maximized by increasing the gripping height, since the sinkage component has negligible impact. With respect to the shape of the leg, this translates into a minimum CoR offset and maximizing the leg radius. As to the mobility (distance covered per consumed Joule), this performance metric is maximized by minimizing the hip height variation, thus the consumed potential energy, and maximizing the distance covered per cycle. For the leg shape this means that it converges to a wheel. Geometrically, in contrast to a leg with an optimal climbing height, the CoR offset needs to be maximized (up to the body height) and the leg radius needs to be minimized up to the asymptote. Thus the biggest conflict regarding the optimal leg shape is the CoR offset.

Analyzing outside the boundaries of the proposed mathematical description, the effect of the trade-off can be superseded by generating a shape that has both a high gripping point and a wheel shape at the rolling segment. This way both design variables are uncoupled and form a leg shape as shown by the example of Figure 17. An important difference of this concept is the definition of climbing height y_c. For the analytical shape description the gripping point was defined as the height where the first derivative is equal to zero (Equation 8 and Figure 6), but for this approach the gripping point is simply the maximum height where the leg (of the second tripod) can hook onto the obstacle (Figure 18).

Although this leg shape is a purely conceptual design, it is interesting to compare the performance with the shapes generated by the analytical description of Section 4.4. This concept has a drawbar pull of 2.1 N (98.9%), a climbing height of 86 mm (101.3%) and a distance covered per Joule of 6.15 m/J (100%). The percentages represent the performance ratio with respect to the feasible maximum of the analytical approach of Section 4.4, whose values are shown in the first row of Table 3. The drawbar pull and distance covered per Joule are equal to the efficient leg's, since this shape is equal to the wheel segment of the conceptual leg. Particularly, the climbing height is higher than the maximum of the analytical case, because the definition of the climbing height is different and apparently higher.

So the conceptual leg does not suffer anymore form the trade-off between climbing and mobility and performs well in both aspects. On average this newly generated shape has a performance ratio of 100.3% with respect to the analytical case, where the maximum average performance of the analytical approach is 84.5%.

Another design aspect that needs to be considered is sinkage during the transition period between two tripods. The results of this are also included in the conceptual leg of Figure 17, in the form of the contact surface tips curling inward. If the contact surface would only consist of the wheel segment, it would dig into the soil due to sinkage. This leads to an abrupt engagement of the alternating legs compromising the stability. In addition, the soil is scooped up, which is even a significant problem for the case of the Lunar Zebro because the top layer's fine fraction of the regolith (classified as lunar dust) poses all kinds of problems for planetary rovers.

Another reason for the decreased radius of curvature at the tips is the transition from one tripod to the other. Whereas on grounds with no or negligible sinkage the transfer moment happens instantly, on compactive soils this transition period is continuous due to the present sinkage. In order to keep the hip height on a constant level, like the wheel segment, the inward curling tips are needed. Without tips the contact area increases during the transition period, the total sinkage is lower and the hip moves upward, which results in an increased energy consumption.
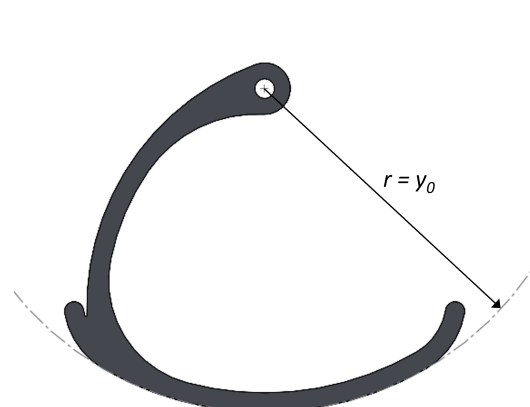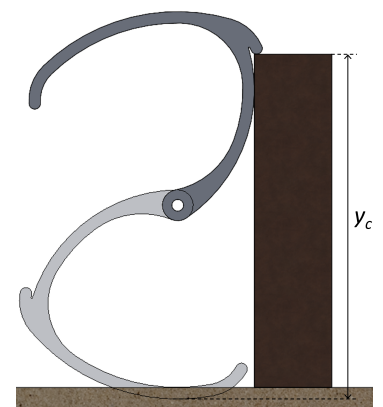

Figure 17. Conceptually generated leg shape

Figure 18. and its climbing height.

5. Discussion

The principal advantages of the proposed model are the system level approach and the leg shape as the basis for analyzing and optimizing a C-legged hexapod's performance. Whereas in previous work the performance aspects (traction, climbing and mobility) were analyzed separately, one can now examine the combined effect. This way the legs of a hexapod can be designed more accurately and applied to an actual rover since the performance aspects also interact in practice. Not only are the performance trade-offs investigated, but also the system's constraints bounding the outcomes. In particular, the representation of the feasible design space that was developed (Figure 11) can be very useful for designers. Besides, not only can the leg shape parameters' impact on the performance be investigated, but other parameters like soil properties and vehicle parameters can be examined or used as design variables.

The proposed analysis is set up for small C-shape hexapods walking at a moderate speed on compactive soils. Yet the application could be extended, since the essence of the model is general; it only needs to be adapted and extended for the intended purpose. To analyze hexapods with increased size and weight for example, additional resistances like leg inertia and bulldozing should be included. For faster hexapods the kinetic energy is not negligible anymore and should be included. Also, to apply the method to other grounds than compactive soils, other traction descriptions corresponding to the surface type should be employed. Considering a hard surface for example, the classical dry friction laws must be used. For a leg moving under extreme sinkage, the soil acts as a transition state of solid and fluid and the hexapod shows swimming-like behaviour [23]. Consequently, the terramechanics models are not valid anymore and resistive force theory should be used [10].

Regarding the manual leg shape optimization of Section 4, the application of the system level model, two aspects are noteworthy. Firstly, the shape description as illustrated by Figure 4 is chosen to implement. However, different leg shapes having 1 DoF can be used as an input by adapting the definitions. Elliptic and polynomial shapes were examined during this research for example, but yielded - particularly with respect to mobility - worse results than the circular shape.

In addition to this, not every performance aspect has equal importance for the operation of the vehicle. Consequently, weight factors could be incorporated. So it is evident to reflect in advance on the operations the rover must execute with the accessory performance requirements. For the exploration of the lunar surface for example, the operation speed is less essential. With this in mind one could lower the weight factor for mobility which influences the outcome of the optimal leg shape.

As to the accuracy of the model, first and foremost it is not experimentally validated. Since the model is meant as a tool to analytically design legs that are used in practice, it is important that the results are validated. In this case the described trends must be verified, since the analysis is comparative and the relative performance is modelled.

Besides, the model is subject to assumptions that decrease the accuracy. The most prominent assumption is the use of a quasi-static model ignoring dynamic effects such as slip. However, it is not the goal of this research to predict the exact performance of leg shapes, but rather the difference between them; the trends and behavior of the underlying physics. Nevertheless, when including slip, these trends could be influenced resulting in different conclusions with respect to the comparative performance analysis. As to traction, soil failure occurs at a lower shear stress regarding a slipping leg [24], so it decreases the maximum thrust the soil can provide. Moreover, the shape of the stress profiles changes [25]; particularly the location of the maxima are not located beneath the lowest point of the wheel, but in front of the wheel, resulting in a higher compaction resistance. As to sinkage, slip is responsible for - on top of static sinkage - the additional dynamic sinkage. The higher the slip, the higher the dynamic sinkage resulting in an increase of the compaction

resistance. With regards to mobility, next to increasing the compaction energy, slip also leads to a decreased distance traveled per cycle which results in a decreased η_x. Hence investigating the influence of leg shapes on the amount of slip could also improve the relative performance.

The climbing height analysis is also an aspect that could be improved. If the unpredictable behaviour of climbing could be analyzed in a more detailed manner, it would improve the accuracy of the model. Besides, in this paper the climbing gait of the Lunar Zebro is used relying on the gripping point, whereas other climbing gaits like the one proposed by Song et al. [26] approaches the obstacle the other way around hooking onto the obstacle and yielding better results. These aspects could introduce constraints based on the maximum motor torque, which has not been considered in the present model.

6. Conclusions and recommendations

In this paper, a system level performance analysis method is proposed to optimize the shape of a C-shape hexapod leg under different conditions. The model describes the combined physical behaviour of the leg's tractive, climbing and mobility performances in a comparative manner and is used to investigate the influence of the leg geometry. A circle segment shape is used as the analytical description of this geometry of which the radius and center of rotation offset (Figure 11) are selected as design variables. A representation including the performance metrics, design variables and constraints is developed to find leg shape optima, which is particularly useful for technical designers.

In the first place it is observed, using the Lunar Zebro as test case, that there is no unique optimal leg shape, but different optima depending on the design and operation requirements. The optimum for traction yields a leg with a maximum radius, resulting in a maximized contact surface. A leg having the highest possible climbing height is formed by a minimized CoR offset and a maximized radius (full C-shape) within the space constraint, resulting in the highest gripping point. The most efficient leg contains a radius and CoR offset equal to the body height (wheel segment), leading to a zero hip height variation.

Having no unique optimum, the system level performance of these different leg types, measured by the average ratio with respect to the feasible maxima, also don't differ significantly. The efficient and tractive leg perform best on average; ~8% higher compared to the climbing, all-round (having an intermediate shape) and Lunar Zebro leg (tending to the full C-shape of the climbing leg). The main reason for this insignificance is the trade-off between climbing and mobility.

Analyses with other conditions, like normal weight, soil parameters and pressure-sinkage relationship show no significant changes with respect to the general results of the performance ratio. Another relevant observation is the fact that almost every leg type uses the maximum available space. Subsequently, the nominal speed also increases for legs having a larger effective radius. So a larger vehicle is faster and has a higher performance regarding the three metrics. Although, the size is bounded seeing that the mass will also increase.

Coming back to the proposals stated in Section 1, the research goal is met in general and several judgements can be made. Firstly, the proposed method to describe a C-leg's performance on system level is developed and found to be useful especially for designers, due to the comparative nature. The model is not suited to exactly predict the performance, but the order of magnitude is sufficient to quantify the relative performance of different leg shapes. Initially it was hypothesized that the commonly used full C-leg could be improved and that a more optimal shape would be generated. The former was found to be true, seeing the described results. One unique optimum however, was not found using the analytical method due to the trade-offs between the three performance metrics. But more importantly, the several optima are possible depending on the design and operation requirements. The leg shape optimization is limited by the shape description, but the model

provides insight in the relationship between shape and performance. Accordingly, leg shapes can be generated using this fundamental knowledge, with Figure 17 as an example. This concept performs 16% better (average relative performance) compared to the efficient and tractive leg of the main case. The crux of this concept is the increased climbing height being determined by the shape hooking onto the obstacle instead of gripping and still having maximum mobility due to wheel shape at the contact surface.

There is still a lot to investigate in the domain of the up-and-coming C-shape legged rovers. Regarding this research, the novel system level performance analysis method is promising, but can be further extended and improved to effectuate wide application.

Firstly, the provided trends and results should be experimentally validated. Also, multiple aspects discussed can improve the accuracy of the model, with the incorporation of slip in particular. The dynamic sinkage and its implications should be paid intention to in that case.

As described in Section 1 most of the work done with respect to C-legged rovers is based on gait and control, whereas this paper uses the leg shape as a starting point. The former uses a predetermined leg shape and optimizes the gait, while this work uses a predetermined gait (or assumes the gait can be fit to the legs) and optimizes the leg shape. Both approaches are relevant, but it would be ideal to incorporate both in a parallel manner.

Regarding traction, compliant legs can be an aspect worth investigating. It improves the stability, shock absorbance and could serve as suspension. Having a deformable contact surface also increases the drawbar pull according to Cardile et al. [14]. Lastly, the potential energy during every cycle is being dissipated, but with energy regeneration during the 'descent' of the hip trajectory the energy consumption could be decreased.

Abbreviations

UGV	Unmanned ground vehicle
LZ	Lunar Zebro
CoR	Center of rotation
DoF	Degree of freedom
TM	Terramechanics

Nomenclature

α	Leg angle
α_c	Ground contact leg angle
$\alpha_{\min}$	Vertical minimum leg angle
β	Roation angle
β_c	Ground contact angle
β_r	Recovery angle
β_w	Walking angle
Δy	Hip height variation
$\hat{k}$	Meirion-Griffith sinkage modulus
$\hat{m}$	Diameter exponent
$\hat{n}$	Meirion-Griffith sinkage exponent
ω_m	Maximum angular motor speed
ω_w	Angular leg speed during walking step
ω_w	Angular leg speed in walking period
ϕ	Coulombian angle of internal friction
σ	Soil normal stress
τ	Soil shear stress
θ	Arbitrary angle along wheel/leg-soil contact
θ_1	Sinkage angle
$\vec{P}_i$	Position of a point on leg in starting configuration
$\vec{P}_p$	Position of a point on leg in recovery period
b	Wheel/leg width

c	Coulombian angle of internal cohesion
D	Wheel/leg diameter
DP	Drawbar pull
E_g	Gravitational energy
E_r	Consumed compaction energy
F	Maximum soil thrust
g	Gravitational acceleration
i	Gearbox transmission ratio
k	Sinkage modulus
k_ϕ	Bekker frictional sinkage modulus
k_c	Bekker cohesive sinkage modulus
m	Vehicle mass
m_l	Leg carrying mass
N	Normal force acting on single leg
n	Bernstein–Goriatchkin sinkage exponent
R	Soil motion resistance
r	Wheel/leg radius
r_0	Maximum available space
r_e	Effective leg radius

s	Arc length over which leg has rolled
t_w	Walking time
$v_{\min}$	Minimum nominal velocity
W	Leg carrying weight
x	x-coordinate
x_c	x-coordinate of ground contact instance
x_i	Initial x-coordinate
x_t	Horizontal rolling tranlation
x_{total}	Distance covered per cycle
y'	Gripping point
y	y-coordinate
y_0	Body height
y_c	Climbing height
y_i	Initial y-coordinate
y_s	Distance between CoR and circular center
y_t	Vertical rolling tranlation
y_{off}	Vertical CoR offset
z	Wheel/leg sinkage
z_0	Total sinkage

Appendix A

Table A1. Constant values and range of the input parameters, used for the sensitivity analysis in Section 3. Vehicle constants are LZ based exemplary values, environmental constants[1] are retrieved from [21]. Vehicle parameter ranges are based on the scope of this paper (hexapods < 5 kg), environmental parameter ranges on general boundaries present on Earth and the Moon.

Parameter	Constant	Range
r (mm)	30	10 - 60
y_{off} (mm)	0	0 - 60
y_0 (mm)	50	0 - 60
b (mm)	20	5 - 50
c (kPa)	0.52[1]	0.5 - 4
ϕ $(°)$	42[1]	20 - 50
n $(-)$	1[1]	0.7 - 1.3
k_c (kPa/m^{n-1})	1.4[1]	0.5 - 1.5
k_ϕ (kPa/m^n)	820[1]	500 - 3000
m_v (kg)	2.5	0.5 - 5
g (m/s^2)	1.635	1 - 10

(a) $y_0 = 30\,mm$

(b) $y_0 = 40\,mm$

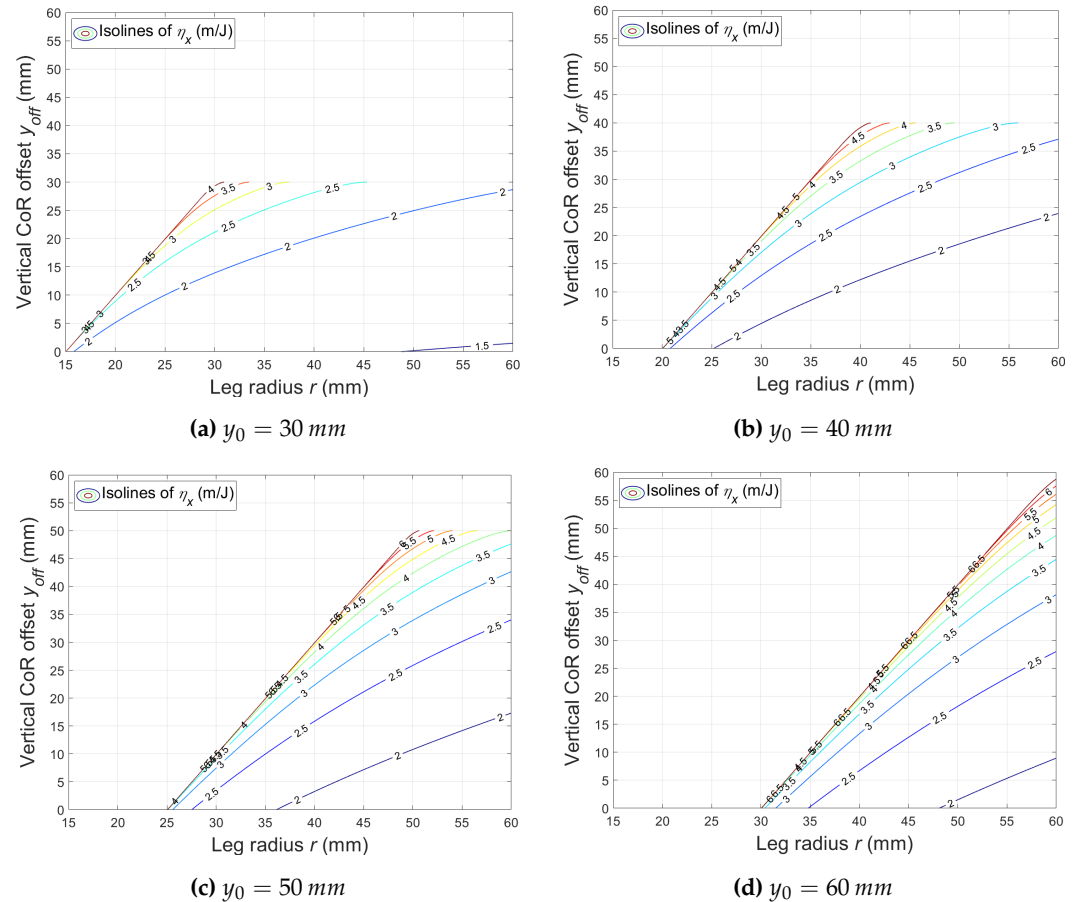**(c)** $y_0 = 50\,mm$

(d) $y_0 = 60\,mm$

Figure A1. Distance covered per Joule η_x (mobility) as a function of leg radius r and CoR offset y_{off}, with a varying body height y_0. The input parameters and conditions of Section 4.1 are used.
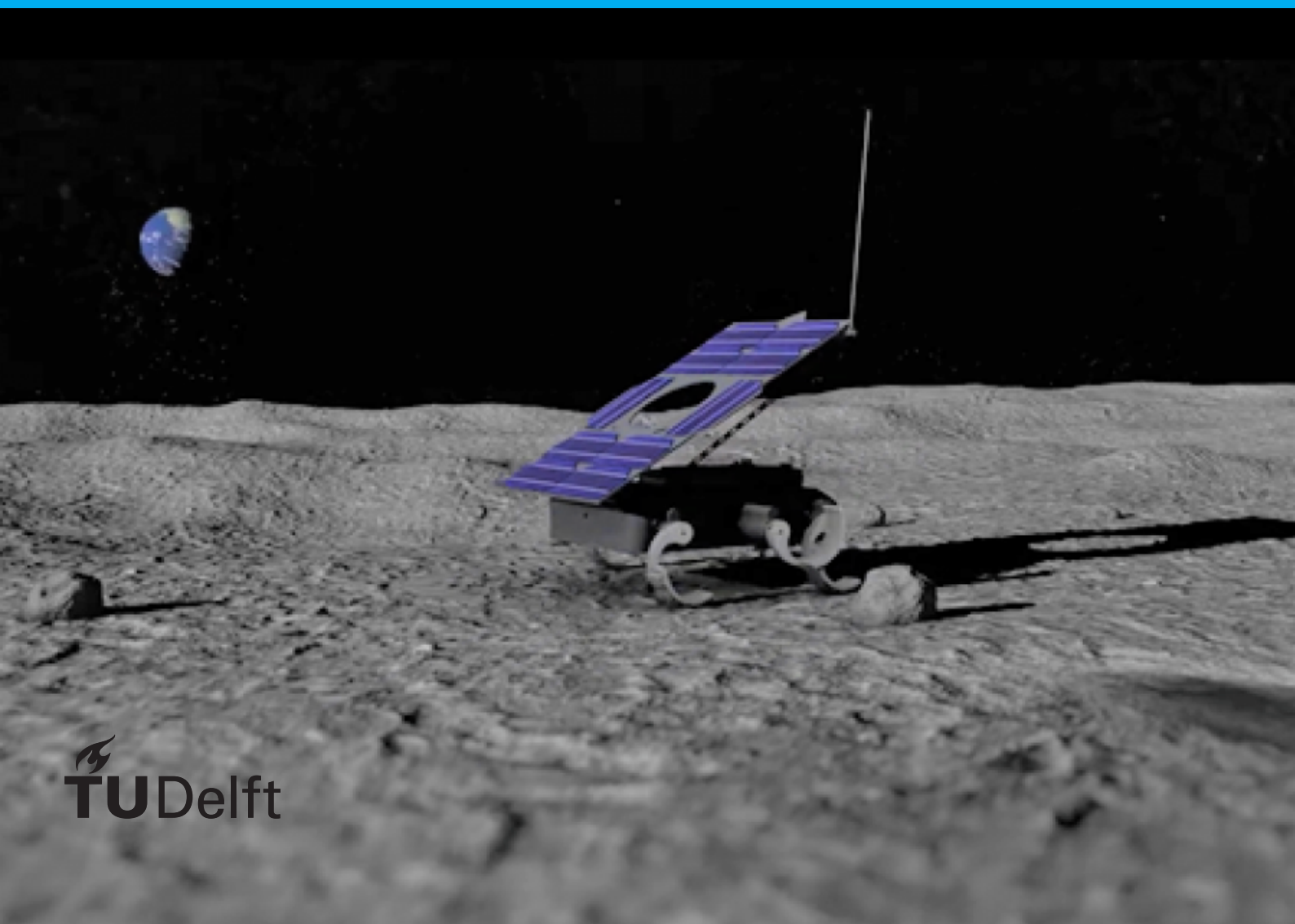
References

1. Bruzzone, L.; Quaglia, G. Review article: Locomotion systems for ground mobile robots in unstructured environments. *Mechanical Sciences* **2012**, *3*, 49–62. doi:10.5194/ms-3-49-2012.
2. Boston Dynamics.
3. TU Delft Space Institute.
4. AutomationSR.
5. Lunar Zebro.
6. Saranli, U.; Buehler, M.; Koditschek, D.E. RHex: A simple and highly mobile hexapod robot. *International Journal of Robotics Research* **2001**, *20*, 616–631. doi:10.1177/02783640122067570.
7. Goldman, D.; Komsuoglu, H.; Koditschek, D. March of the sandbots. *IEEE Spectrum* **2009**, *46*, 30–35. doi:10.1109/MSPEC.2009.4808384.
8. Zebro.
9. Xu, L.; Liang, X.; Xu, M.; Liu, B.; Zhang, S. Interplay of theory and experiment in analysis of the advantage of the novel semi-elliptical leg moving on loose soil. *2013 IEEE/ASME International Conference on Advanced Intelligent Mechatronics: Mechatronics for Human Wellbeing, AIM 2013* **2013**, pp. 26–31. doi:10.1109/AIM.2013.6584063.
10. Li, C.; Zhang, T.; Goldman, D.I. A Terradynamics of Legged Locomotion on Granular Media **2013**. *339*, 1408–1413.
11. Moore, E.Z. Leg Design and Stair Climbing Control for the RHex Robotic Hexapod. *Spring* **2002**, pp. 1–91.
12. Vina, A.; Barrientos, A. C-legged hexapod robot design guidelines based on energy analysis. *Applied Sciences (Switzerland)* **2021**, *11*. doi:10.3390/app11062513.
13. Bekker, M. *Theory of Land Locomotion*; 1960. doi:10.3998/mpub.9690401.
14. Cardilea, D.; Viola, N.; Chiesab, S.; Rougierb, A. Applied design methodology for lunar rover elastic wheel. *Acta Astronautica* **2012**, *81*, 1–11. doi:10.1016/j.actaastro.2012.06.002.
15. Meirion-griffith, G.; Spenko, M. A Comprehensive Pressure-Sinkage Model for Small-Wheeled Unmanned Ground Vehicles on Dilative , Deformable Terrain **2012**. pp. 4052–4057.
16. Oxford Languages.
17. Wong, J.Y.; Reece, A. PREDICTION OF RIGID WHEEL PERFORMANCE BASED ON THE ANALYSIS OF SOIL-WHEEL STRESSES PART I. PERFORMANCE OF DRIVEN RIGID WHEELS, 1967.

18.   Meirion-griffith, G.; Spenko, M. A pressure-sinkage model for small-diameter wheels on compactive , deformable terrain. *Journal of Terramechanics* **2013**, *50*, 37–44. doi:10.1016/j.jterra.2012.05.003.

19.   Patel, N.; Scott, G.P.; Ellery, A. Application of bekker theory for planetary exploration through wheeled, tracked and legged vehicle locomotion. *A Collection of Technical Papers - AIAA Space 2004 Conference and Exposition* **2004**, *3*, 2109–2117. doi:10.2514/6.2004-6091.

20.   Bernstein, R. Probleme zur experimentellen motorpflugmechanik. *Der Motorwagen* **1913**, *16*.

21.   HEIKEN, G.H.; VANIMAN, D.T.; FRENCH, B.M. Lunar Sourcebook. *Cambridge University Press* **1991**, p. 778.

22.   Jia, Z.; Smith, W.; Peng, H. Fast analytical models of wheeled locomotion in deformable terrain for mobile robots. *Robotica* **2013**, *31*, 35–53. doi:10.1017/S0263574712000069.

23.   Li, C.; Hsieh, S.T.; Goldman, D.I. Multi-functional foot use during running in the zebra-tailed lizard (Callisaurus draconoides) **2012**. pp. 3293–3308. doi:10.1242/jeb.061937.

24.   Janosi, Z.; Hanamoto, B. Analytical determination of drawbar pull as a function of slip for tracked vehicle in deformable soils. *Proceedings of the 1st International Conference of Terrain Vehicle Systems* **1961**.

25.   Wong, J.Y. *Theory of Ground Vehicles*; 2001.

26.   Song, X.; Zhang, X.; Meng, X.; Chen, C. Gait optimization of step climbing for a hexapod robot **2022**. pp. 55–68. doi:10.1002/rob.22037.

A system level performance analysis method for the design of a C-shape hexapod leg operating on compactive terrain

Supplementary materials

J. van Rijn

Contents

1

Background

1.1. Lunar Zebro

Humand kind is eternally fascinated by the universe, the space outside our planet. For the exploration of planets, robot swarms will be deployed in the future, since these networks of explorers can cover a much greater area than one single rover. The rovers in these swarms are an order of magnitude smaller than the current (single) rovers that are deployed on the Moon and Mars. With this miniaturization comes the challenge of engineering a nano rover. The bedrock of the moon and Mars is covered with regolith, a layer of unconsolidated material, which consists of dust and broken rocks. The wheels are the major problem of using the design of a conventional rover and downscaling it to a nanorover. The diameter of the wheels of a nano rover are too small to be able to overcome obstacles like these broken rocks.

The Lunar Zebro, developed by the TU Delft, is a solution to this problem for deploypment on the Moon. This hexapod nano rover has (six) legs instead of wheels and can move in a walking motion on the lunar surface. It is based on the Zebro design [1, 2], which on its turn is based on the Rhex design [3]. However, the Zebro and the Rhex are developed for terrestrial application. Since 2017, the Lunar Zebro team has succesfully developed a nano rover for lunar conditions. A complete redesign with space proof materials is performed with, for example, the addition of a foldable solar panel and sealing of sensitive components against the lunar dust. The above mentioned legs of this hexapod rover are also crucial for the performance of the Lunar Zebro. The legs need to have sufficient traction to traverse slopes and obstacles, and at the same time the motion resistances need to be as low as possible for an optimal efficiency. Due to - with the launch date of mid 2022 in mind - the limited time the Lunar Zebro team has and has had, the legs of the lunar rover can be improved. The current legs are adopted from the Rhex, whereas this robot is designed for the terrestrial environment. In other words, the current legs of Lunar Zebro are not fundamentally designed to operate in the lunar environment.

Zebro originates from the Dutch '**Ze**sb**enige ro**bot', which means six legged robot. The Zebro platform has produced a lot of different prototypes, among which the Lunar Zebro. It weighs 1 kg, has an upright height of around 10 cm and has about the size of an A4 paper. It will travel to the Moon as be a payload of the ISRO Chandryaan-3 mission in 2023.

Six-legged robots have earned a lot of interest in literature because of their ability to climb obstacles and steep slopes - in contrast to wheeled vehicles. Rhex was the first significant project that developed a hexapod robot and is used in a lot of subsequent literature as a reference. The multi-university project originated from the DARPA CBS/CBBS program in 1998 with a funding of 5 million US dollars over five years. In 1999, the first prototype was built by Uluc Saranli and many prototypes, revisions and new hexapod robot projects followed, among which the first commercial Rhex by Boston Dynamics in 2007 and the development of the Zebro by TU Delft since 2012, which this report is based on. The Zebro is, like most Rhex prototypes, also equipped with C-shape legs.

1.2. Lunar environment

For the development of a lunar rover, it is essential to understand the lunar conditions; and for the leg module specifically to understand the nature of the lunar surface. In this section, firstly a brief description of the

lunar environment will be presented, whereafter a more extensive description of the lunar surface and lunar regolith is given. All information is gathered from [4] and [5].

1.2.1. Lunar conditions

The Moon is the only natural satellite (i.e. moon) of Earth and is about one quarter of the size of Earth, which is comparable to the width of Australia. It is the largest moon relative to the size of its planet and one of five biggest moons in the Solar System. The Moon's mass and gravity are about 80 and 6 times smaller than Earth's, respectively. Because of tidal locking, the rotation of the Moon around its axis and its orbit around Earth takes the same time, which is the synodic period (i.e. lunar day) of 29,5 Earth days. This phenomenon is also known as synchronous rotation. Because the Moon and Earth rotate synchronously, the same side of the Moon is always faced to Earth (the near side) and the same side is always faced away from Earth (the far side). There is no significant atmosphere on the moon, which is considered an exosphere. The atmospheric pressure is in the order of magnitude of vacuum on Earth. Therefore, it can not insulate the surface nor trap heat, which is the reason why the temperatures range widely. The temperature on the Moon's surface varies greatly depending on the latitude and whether there is illumination of the sun or not. The lowest temperature measured is only -248 degrees Celsius in a north pole crater by the Diviner instrument on NASA's Lunar Reconnaissance Orbiter in 2009; the highest temperature measured is 127 degrees Celsius at the equator. With regard to the magnetic field, the Moon practically has none, but some of its surface rocks exhibit remanent magnetism from the time the Moon actually had a magnetic field compared to Earth nowadays.

1.2.2. The surface of the Moon

As mentioned, the nature of the lunar surface is essential for the design of a lunar rover. Because of the lack of atmosphere, the surface is greatly bombarded by asteroids and laced with impact craters (figure 1.2). These craters are the most characteristic feature of the lunar surface. They can vary from microns to tens of kilometers in size and have depths of meters to hundreds of meters. Walls in old craters can be up to 10 to 15 degrees, where in younger craters the walls can be up to 40 to 45 degrees.

The lunar landscape can be divided into the more ancient rugged highlands called terrae and the younger lowlands called maria. In figure 1.1 the highlands are the light areas and lowlands the dark areas. The maximum height difference measured is about 18 km between the lowest and highest point on the lunar surface. The terrae consist of plains between hills and furrowed mountainous areas of anorthosite rich in calcium and aluminum. The maria are more smooth than the cratered highlands and concentrated on the near side. These basins are vast solidified pools of basaltic lava rich in iron and magnesium, formed by ancient volcanic eruptions. Since the volcanic period - and thus the formation of the maria - happened in a later stage than the formation of the highlands, the maria are less cratered and more smooth than the highlands. This is simply because the period of bombardment has been shorter.

Apart from these two main landscapes, some geological features exist on the Moon which characterize the surface. Craters are the most common and occuring feature on the Moon, as described above. Other relevant features are rilles, wrinkle ridges, domes and lava tubes.

Rilles are deep channels formed by volcanic activity in the maria and 'cut' the surface. They vary in size

Figure 1.1: The near side of the moon
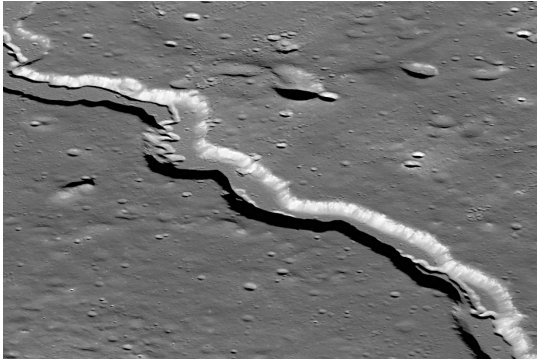

Figure 1.2: Impact craters

Figure 1.3: Rille

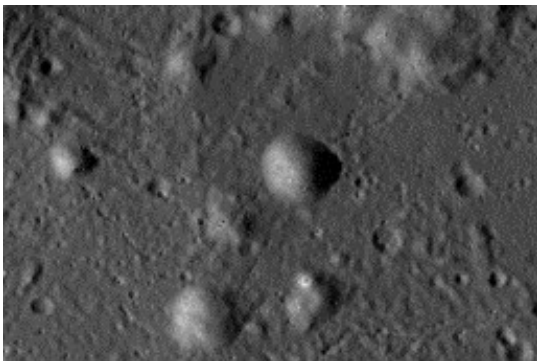Figure 1.4: Wrinkle ridges

Figure 1.5: Domes

Figure 1.6: The 'skylight' of a lava tube

from a few kilometers to 300 km in length, from tens of meters to 3 km in width and have a mean depth of about 100 m (figure 1.3).

Wrinkle ridges are (sinuous) ridges and were formed in the maria when the basaltic lava cooled and contracted. These tectonic features buckle the surface and are on average a few kilometers wide and a few hundreds of meters high (figure 1.4).

Domes are a type of shield volcano found on the Moon. They originated from eruptions in local vents, whereafter slow cooling occurs. The center elevates up to a few hundred meters and the diameters is typically 8 to 12 km. So these features contain really gentle slopes (figure 1.5).

Lava tubes are formed during eruptions of basaltic flows and are hollow underground channels. They can be up to 500 m in diameter and several kilometers in length. Sometimes these tubes are visible when revealed by a 'skylight', which is a part of the roof that collapsed. Lava tubes are a current topic of interest in research, because they can provide human shelter against cosmic radiation, solar radiation and meteorites. The environment inside these tunnels is also more stable in a sense that the temperature fluctuates significantly less: around -20 degrees Celsius. It is also believed that they could lead to Moon caves, which could provide even more human shelter (figure 1.6).

1.2.3. Lunar regolith

Almost the complete surface of the Moon is covered with a layer of unconsolidated solid rock, called lunar regolith. It originates form the Greek word 'rhegos' and 'lithos', which mean blanket and rock respectively. This 'blanket of rocks' has formed from the impact of large and small meteoroids, from the steady bombardment of micrometeoroids and from solar and galactic charged particles breaking down and pulverizing surface rocks. In the maria and the highlands the regolith is generally 4 to 5 meters and 10 to 15 meters thick, respectively. Underneath the regolith layer is a region of coarser fractured bedrock, which is often referred to as 'megaregolith'. Rarely, at steep-sided crater walls, there is no regolith and the bedrock is visible.

As to the composition, lunar regolith is constructed from minerals and glasses that formed under negligible oxygen partial pressure and in the absence of water. Minerals are solid crystalline solutions. Only four

minerals — plagioclase feldspar, pyroxene, olivine, and ilmenite — comprise over 98% of the lunar crust. A more detailed chemical composition can be found in [5].

On the surface of the Moon the size of the particles of the regolith varies greatly. It can be subdivided into three types by the particle diameter: dust (<30 μm), soil (30 μm - 1 cm) amd boulders (>1 cm). Analyses of the returned samples have concluded that the bulk of the lunar regolith consists of particles which are smaller than 1 cm. In the research field this fine-grained fraction is categorized and called lunar soil. The regolith consists to a lesser extent of larger size particles in the shape of boulders. The finest fraction is the lunar dust, which is a challenging factor during missions. Because of the adhesive properties it accumulates on for example optical and heating equipment, which can lead to limited vision and overheating problems. For the wheels and legs per se, the dust does not create problems necessarily.
So for the analysis of the basic traversing behaviour of legs and wheels on the surface of the Moon the lunar soil is the part of the spectrum which is used. It must be noted that the boulders become relevant when one looks at the climbing behaviour and the negotiation of obstacles. Although the chemical compositions of the lunar soil varies greatly, physical bulk properties like density and cohesion are rather uniform over the surface. [4] and [6] are used as references for the geophyiscal properties of lunar soil, of which the relevant ones are shown in table 1.1.

Table 1.1

(Geo)physical properties of lunar soil. Values are averages over a depth of 0 - 15 cm. [4][6]

Physical property	Quantity	Numerical value	Unit
Density	ρ	1.4	g/cm^3
Coulombian angle of internal friction	ϕ	42	°
Coulombian coefficient of cohesion	c	0.52	kPa
Coefficient of rolling resistance	f	0.025	-

1.3. Planetary rovers

Planetary rovers are (un)manned ground vehicles which traverse on a body in space other than earth. Up to now only the Moon and Mars are explored by these carts. In table 1.2 an overview of the rovers which were successfully deployed is given [5]. Rover missions to Mars are also reported, since the Martian terrain is very similar to the lunar terrain, where a layer of fine-grained regolith also covers the planet. To classify planetary rovers by size, a distinction is made by weight [5]:

- Macro rovers (>150 kg)

- Mini rovers (30-150 kg)

- Micro rovers (5-30 kg)

- Nano rovers (<5 kg)

All deployed rovers yet are wheeled vehicles, with either four, six or eight wheels. Moreover, the smallest rover weighs 11.2 kg (Sojourner, 1997), so no nano rover is deployed yet. Although this project aims on a legged nano rover, lessons can be learned from these missions with regard to design principles. The same holds for rovers on Mars, where the conditions are different from the Moon. On Mars however, similar conditions apply with the planet also being covered with loose (Martian) regolith. Apart from planetary rovers that went on a successful mission, some missions of built rovers were cancelled or failed. On one of those failed missions the only non-wheeled rover was planned to drive on Mars during the Russian Mars 3 mission. This unique rover, also the only built nano rover, used a pair of skis mounted onto legs. In the following sections, some relevant lessons learned from rover missions are described [4][5].

Lunokhod 1 & 2
In 1970 and 1973, during the Russian Luna 17 and 21 missions, two macro rovers landed on the Moon. These eighth-wheeled rovers, Lunokhod 1 and 2, were the first planetary rovers and weighed about 800 kg. The design of both rovers was practically the same, apart from an improved control system and TV camera

Table 1.2: Overview of deployed planetary rovers

| Rover(s)	Year of launch	Location	Weight (class)	Particularities
Lunokhod 1 & 2	1970	Moon	756 kg (macro)	First planetary rover
LRV 15, 16 & 17	1971 - 1972	Moon	708 kg (macro)	Manned rovers
Prop-M rovers*	1971	Mars	4.5 kg (nano)	Ski rover, missions failed
Sojourner	1997	Mars	11 kg (micro)	First rover on Mars
Spirit & Opportunity	2004	Mars	174 kg (macro)	
Curiosity	2012	Mars	900 kg (macro)	
Yutu 1 & 2	2013, 2018	Moon	120 kg (mini)	First rover on the Far Side
Pragyan*	2019	Moon	27 kg (micro)	Mission failed
Perseverance	2020	Mars	1025 kg (macro)	
Zhurong	2020	Mars	240 kg (macro)	
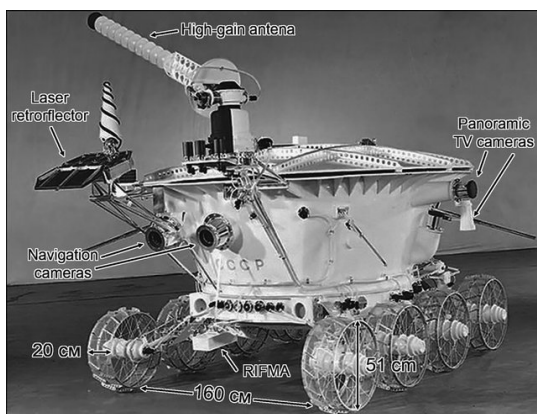
Figure 1.7: Lunokhod-1 lunar rover

Figure 1.8: Lunokhod wheel

configuration for the 84 kg heavier second rover. They were able to drive up to 2 km/h, overcome a step height of 0.35 m and navigated by skid steering. Eight wheels were implemented in the design to the minimize the wheel size while keeping high traction. A ninth unpowered trailing wheel was used to measure the actual speed and distance since it did not slip. The 2.7 kg driving wheels were rigid spoked wheels with a diameter of 51 cm and a width of 20 cm. The rims consisted of a reinforced wire carcass with 2 cm high cleats for traction (negligible coverage).

The Lunokhod-1 mission ended, after driving 11 km during eleven months (average speed of 0.14 km/h) over Mare Imbrium, when the radioisotope failed and the internal temperature could no longer be maintained. The Lunokhod-2 mission ended after driving 37 km during eight weeks (average speed of 0.34 km/h) over the more rugged Mare Imbrium. The operators overlooked a crater and the vehicle tumbled over the edge, but at first sight it recovered from the fall. However, due to the fall lunar dust had accumulated on the heater and the mission failed due to overheating.

Lunar Roving Vehicles

Between 1971-1972 the USA performed the Apollo 15,16 and 17 missions, each with a lunar rover called LRV (Lunar Roving Vehicle). These macro rovers were not UGV's, but had to be operated on board by astronauts with a joystick, but could also be teleoperated if necessary. Its function was to transport astronauts and their measurement equipment to the designated locations. The three LRV's differed insignificantly from each other. Fully loaded the four-wheeled vehicles weighed about 700 kg. They were able to drive up to 14 km/h, overcome a step height of 0.3 m and navigated by double Ackermann steering. Each independently driven wheel had a diameter of 81.8 cm a width of 22.9 cm and weighed 5.48 kg. The wheels were, in contrast to the Lunokhod's, flexible and deflected 4.5 cm on average. The compliance was accomplished by a wire mesh carcass with stiff inner frames to prevent over-deflection. 50% percent of the tires is covered with V-shaped
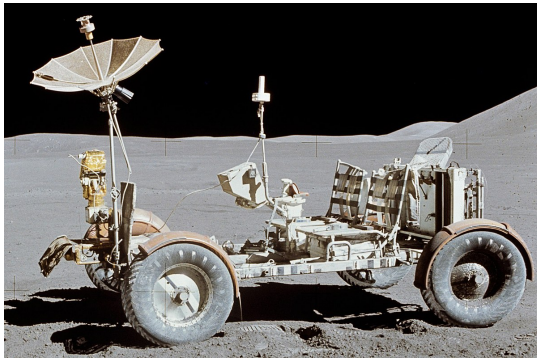
Figure 1.9: Apollo-15 lunar rover (LRV)

Figure 1.10: LRV wheel

strips (chevron treads) of 0.279 mm high that act as grousers.

Although the LRV missions did not fail significantly (the rovers were also part of a bigger mission), the lunar dust also caused problems for the LRV's. During the Apollo 16 mission a fender got lost and the dust was thrown while driving. The dust covered the crew and equipment which resulted in high battery temperature and increased power consumption. A repair attempt is not mentioned, in contrast to the LRV of the Apollo 17 mission. Here a fender also broke when an astronaut bumped it accidentally with a hammer handle. Again the dust accumulated on the equipment and caused heat problems. This time the crew had a practical solution and reconstructed the fender again.

Sojourner

In 1997 NASA's Sojourner rover was the first rover to land on Mars with the Mars Pathfinder mission (MPF). It was also the first planetary rover which was not a macro rover, but even a micro rover of 11.2 kg. Sojourner was solely an experimental vehicle (not exploratory) and did not drive further than 10 m from the MPF lander, with a total covered distance of 106 m. Sojourner was used to test and verify technical solutions for future rovers and research. For example, this was the first rover with a (semi-)automatic navigation system and needed to be tested. Moreover, the effects the Martian dust were tested, which were still quite unknown at that time. So unlike the Lunokhods and the LRV's, it was not meant to operate in varied terrain with obstacles. It needed to be able to traverse on the loose Martian soil layer. It was able to drive at speeds up to 0.6 cm/s with a nominal speed of 0.4 cm/s. This UGV had a six-wheeled rocker-bogie lever chassis, a suspension system which would be used in all subsequent NASA rovers. All wheels are driven independently by tractive motors and four additional motors were employed on the outer wheels for steering. The wheels of the micro rover had a diameter of 12.5 cm and a width of 7.9 cm. The rigid wheels drove on treads with 1 cm protruding cleats of 16 x 0.127 mm.

Spirit and Opportunity

In 2004 NASA deployed two identical macro rovers of 174 kg on two different sites on Mars: Spirit and Curiosity. These rovers were the first to drive significant distances of 7.73 km and 33.2 km respectively. The goal of this mission was to characterize the geology of their landing sites. The chassis was adopted from the Sojourner rover, but in a larger implementation.
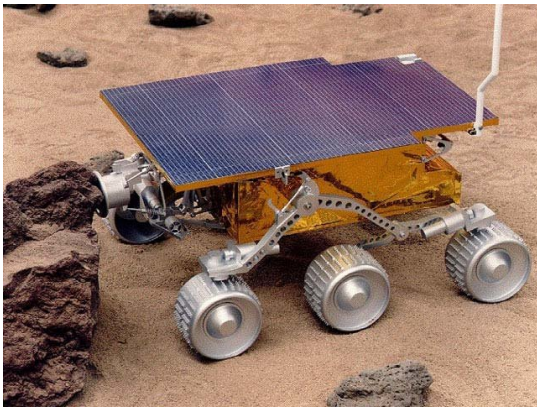
Figure 1.11: Sojourner Martian rover (MPF)
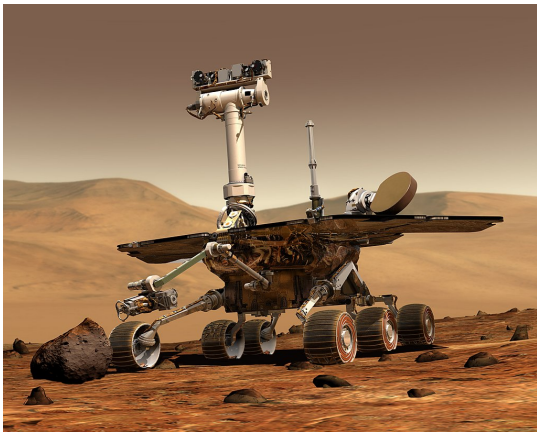

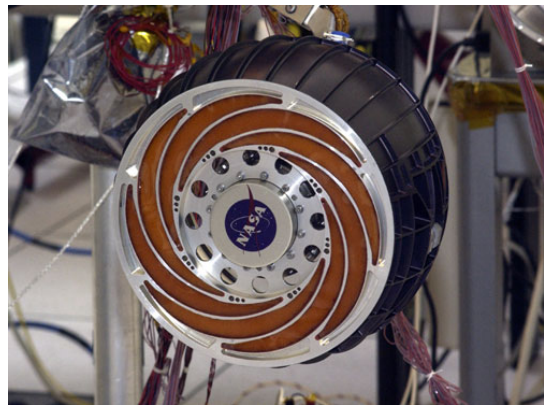Figure 1.12: Sojourner wheel

Figure 1.13: MER Martian rover

Figure 1.14: MER wheel

Figure 1.15: Curiosity Martian rover (MSL)

Figure 1.16: Curiosity wheel

1.4. Legged UGVs

In the past decades the development of mobile robots has grown rapidly. These robots can be classified [7] by the environment in which they move: unmanned air vehicles (UAV), autonomous underwater vehicles (AUV) and unmanned ground vehicles (UGV). The latter is within the category of the scope of this research and can be further classified by the locomotion system: wheeled, tracked and legged.
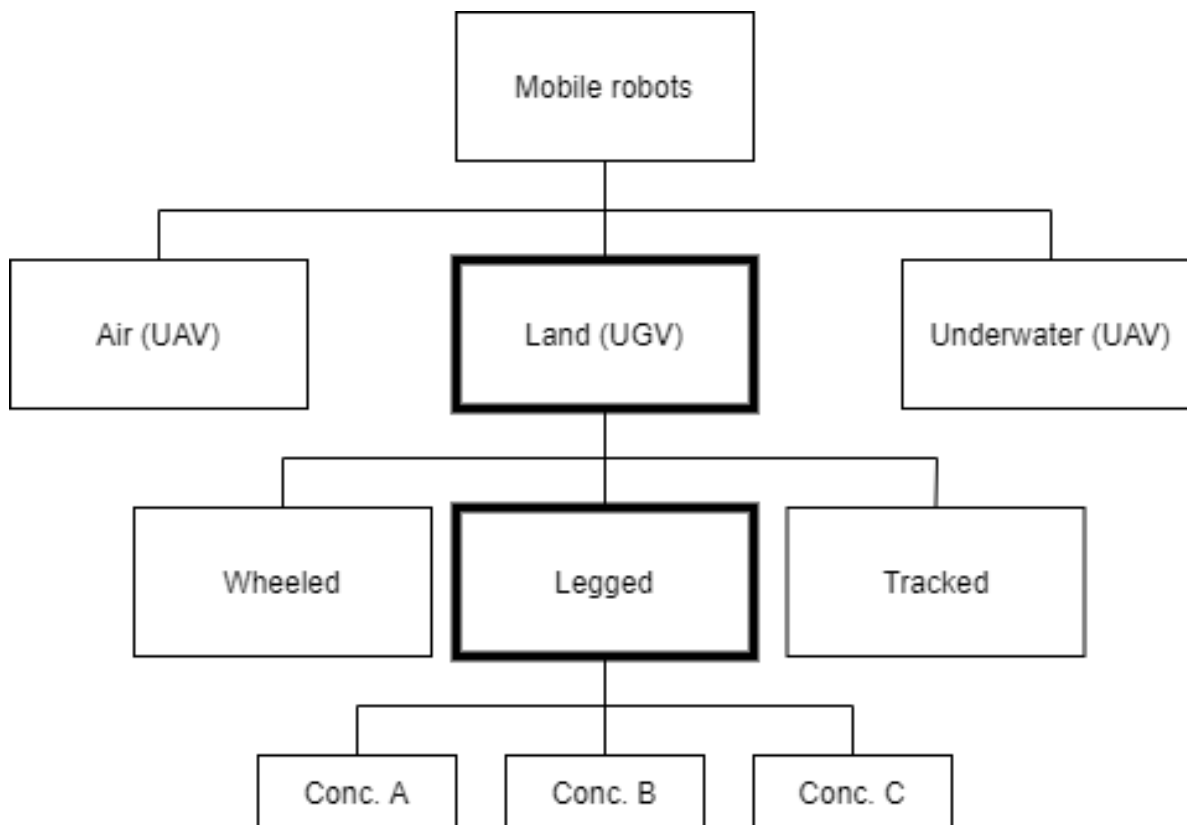

Figure 1.17: The classification of legged robots

1.4.1. Wheeled and tracked vehicles

Wheeled vehicles are most widely used on earth and make up a big part of the ground vehicles. They are known of their ability to drive at high speeds and their high energy efficiency. However, these abilities do not apply for uneven and soft surfaces with obstacles [8]. On significantly irregular terrains wheeled vehicles are even not able to drive. For this manner, tracked and legged vehicles are better suited for soft grounds with obstacles, like the surface of the moon. Tracked vehicles perform well on uneven terrain, but have poor obstacle climbing ability and energy consumption is relatively high [8].

1.4.2. Legged vehicles

Legged vehicles however, have the ability to overcome obstacles. This superior mobility with respect to the other two categories arises from the fact that legged robots do not need a continuous support surface, but use a discrete foothold for each leg, enhancing their mobility [9]. Wheeled and tracked vehicles, on the contrary, require a continuous support surface.

Legged ground vehicles possess more advantages when deployed in unstructured environments. When a legged robot moves in soft surfaces, deserts or regolith for example, the ability to use discrete footholds improves the energy consumption in this manner, since they deform the terrain less than wheeld or tracked vehicles. Therefore, the energy needed to get out the depressions is lower and the contact area among the foot and the ground can be made in such a way that the ground support pressure can be small [10].

Also, the legs can have one or more joints, which increases the mobility since the leg configuration can be

varied. Those joints themselves can also contain multiple degrees of freedom, which enhances the mobility even more [11]. It is also possible to 'vary the body height, introducing a damping and decoupling effect between terrain irregularities and the vehicle body (and as a consequence, its payload)' [11].

Besides, legged vehicles, particularly with six or more legs, have higher failure tolerance than wheeled or tracked vehicles. If one ore more legs are damaged, the mobility is decreased, but the robot can still move, since legged vehicles can contain redundant legs. In opposition, a failure of one of the wheels of a wheeled vehicle cause it to become immobile, because all wheels should be in permanent contact with the ground during locomotion [11]. Also, most legged robots have one actuator per leg. So if an actuator or its control fails, the vehicle is also still mobile in this manner, due to redundancy.

Nonetheless, legged vehicles also have disadvantageous aspects, of which the most significant one is their low speed and energetic inefficiency compared to tracked and, in particular, wheeled vehicles. This is an important drawback in modern robotics as the battery energy-storing capabilities, and their heavy weight is a limiting design criterion [9]. Moreover, generally speaking, legged robots have more actuators, making them heavier, difficult to build (most types) and demand complex control algorithms [11].

1.4.3. C-shape leg
With the acquired knowledge about different types of mobility systems, the reasoning behind the use of C-shape legs can be described. Generally speaking, a C-leg offers a balanced trade-off between the efficiency, simplicity and robustness of wheels and the traversing capabilities of a leg. In contrast to most legs of legged robots, the leg configuration of the Zebro can be varied less than legs with multiple joints. So it has less discrete footholds and therefore a lower obstacle negotiating capability than a multi-joined legged rover. On the other hand less actuators are needed, which makes the Zebro lighter. Compared to a wheeled rover, a C-shape legged rover needs more actuators, because the legs don't move synchronously. The Zebro even needs one actuator per leg, since navigation is performed by skid steering. Moreover, this redundancy because of the remote application in space. In other words, the C-shape leg presents the best of both worlds.

2

Research scope

After the literature study the research proposal was as follows: *Redesign the legs of the Lunar Zebro on basis of terramechanics theory for an optimal traversing capability by shape and compliance.*
In the end the title of the final work (the paper) is as follows: *A system level performance analysis method for the design of a C-shape hexapod leg operating on compactive terrain.*

In this chapter the evolvement of the research scope is described.

So in the first stage of the project the focus was on traction only, because this is the main topic for planetary rovers in literature. Traction is the bottleneck for the success of exploration missions as described in section 1.3. The first sub-goal was to investigate the influence of the leg shape on the drawbar pull for the Lunar Zebro, and to validate the results experimentally. Besides concrete results for the LZ, the results would be compared to see potential differences between the used leg model and the tested legs. First the terramechanics field and all its different models were investigated and the shape description was examined. But in the beginning phase of the project, developing the experimental set-up (described in 3.2), it was already observed a broader performance analysis was needed to be able to generate optimal leg shapes. Namely, from the traction analysis it was apparent that increasing the contact surface increases the drawbar pull.
On this point two different research scope were possible: on the one hand a leg shape and compliance based traction analysis and the validity of the wheel model, on the other hand a system level performance analysis providing design guidelines for a C-shape leg. The latter research scope was chosen to explore, because its generality would have more impact; eventually leading to the choice of writing the paper. Due to the general approach, a scope broader than only the Lunar Zebro on lunar soil is used. The definition of system level performance for an exploration hexapod on compactive ground was examined resulting in not only traction, but also climbing and mobility.

3

Supplementary research

3.1. Terramechanics

In order to investigate the performance of a C-shape leg, this must be quantified by a theoretical physics framework: terramechanics theory. The relevant findings in this research field will be described in this section.

In literature the performance of a planetary rover is generally qualified by the traversing capability: the extent to which it negotiate slopes, obstacles and loose soil. It was found that the efficiency, the distance it can travel in one cycle, is of less importance. The reason for this is the fact that during a rover mission time is not an issue. The limiting factor is the terrain (Chapter 1.2). A good measure for the traversing capability is the drawbar pull, which is the amount of thrust that is left to overcome obstacles, slopes, loose soil or for acceleration. In order for a vehicle to move, the horizontal thrust, also known as traction, has to be larger than the sum of the motion resistances. In other words, the difference between the traction and the motion resistances has to be larger than zero, even if this is minor. However, in practice it is satisfactory if the drawbar pull is sufficiently large for vehicles to overcome slopes and obstacles. The equation for the drawbar pull, which is the governing equation for the performance of a ground vehicle, yields [12]:

$$DP = F - R \tag{3.1}$$

with DP the drawbar pull, F the thrust and R the sum of the motion resistances.

Thus, in literature the drawbar pull is used as a measure of the trafficability of a vehicle, exactly what this project is aiming for. In the first section of this chapter, it is described how to predict the drawbar pull by the Bekker theory, which forms the basis of terramechanics. Thereafter, in the following sections several relevant improvements and extensions for certain application on this model are described.

3.1.1. Bekker theory: the fundament of terramechanics

Around 1960 Bekker [13] introduced a semi-empirical model to estimate the mobility performance of off-road vehicles by predicting the motion resistance and the soil thrust on homogeneous, granular soils (Eq. 3.1). The fundamental equation for this is the so called pressure-sinkage relationship which governs the depth a wheel will sink into the soil when subjected to a vertical load:

$$\sigma = \left(\frac{k_c}{b} + k_\phi \right) z^n \tag{3.2}$$

where σ is the normal stress (i.e. the ground contact pressure), k_c is the modulus of the soil deformation due to the soil cohesive ingredients, k_ϕ is the modulus of the soil deformation due to the soil frictional ingredients, b is the smaller dimension of the contact patch, that is, the width of a rectangular contact area, or the radius of a circular contact area, z is the sinkage and n is the exponent of soil deformation. Bekker based his model on the Bernstein-Goriatchkin equation [14], which goes back to 1913, yielding:

$$\sigma = k z^n \tag{3.3}$$

where k is the sinkage modulus, which is equal to $k_c/b + k_\phi$. So these models imply that the magnitude of the normal stress underneath a wheel scales exponentially with the dimension of the depth z. The shape of the exponential curve is determined by the the pressure-sinkage parameters k_c, k_ϕ and n. These geophysical parameters are determined from field tests by measuring the terrain response with a bevameter. The values can be derived from two of those pressure-sinkage tests with two plates having a different width or radius b. To prevent the effect of possible localized nonhomogeneity, the aspect ratio of such a plate has to be larger than 5 to 7 and the absolute value of b needs to be larger than 10 cm. k_c and k_ϕ can be derived by measuring the pressure at a depth of $z = 1$ for both plates, whereafter n can be determined. A more detailed description can be found in [12]. Important to note is that Bekker assumed that 'the terrain reaction at all points on the contact patch is purely radial, and is equal to the normal pressure beneath a horizontal plate at the same depth in a pressure-sinkage test' [13].
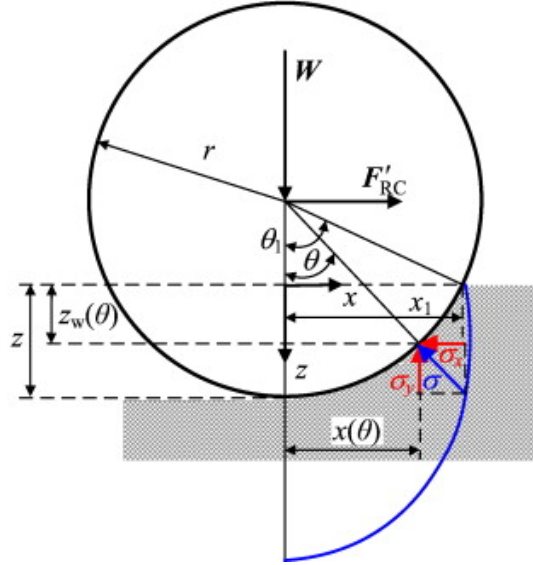

Figure 3.1: Stress distribution according to the Bekker model.
Figure retrieved from [15].

Motion resistance

In figure 3.1 a characterization of the shape of the pressure distribution is given with the blue curve. It can be seen that Bekker assumes that the ground contact area always stops at the 'dead point' of the wheel, the location where z is at its maximum. It is also assumed the maximum soil stress occurs at that point.

Moreover, this figure depicts the free-body-diagram of a wheel on deformable ground. In this case a towed wheel is used to determine the resistance a wheel would experience. The equilibrium in horizontal direction is the balance between the towing force, which equals the motion resistance R experienced, and the horizontal normal force:

$$R - \int_0^{\theta_0} dN \sin\theta = 0 \qquad (3.4)$$

where θ_0 is the soil entry angle, θ is an arbitrary angle along the wheel-soil contact arc and dN the elementary normal force.

The equilibrium in vertical direction is the balance between the vertical wheel load and the vertical normal force:

$$-W + \int_0^{\theta_0} dN \cos\theta = 0 \qquad (3.5)$$

where W is the vertical load.

The elementary normal forces can be expressed in terms of the normal stress and the rectangular coordinates.

$$dN \sin\theta = b\sigma r \sin\theta \, d\theta = b\sigma \, dz \tag{3.6a}$$

$$dN \cos\theta = b\sigma r \cos\theta \, d\theta = b\sigma \, dx \tag{3.6b}$$

where r is the wheel radius.

Substituting Eq. 3.6a and Eq. 3.6b in Eq. 3.4 and Eq. 3.5 respectively, and subsequently substituting the pressure-sinkage relationship (Eq. 3.2) yields:

$$R = b \int_0^{z_0} \left(\frac{k_c}{b} + k_\phi \right) z^n \, dz = b \left(\frac{k_c}{b} + k_\phi \right) \frac{z_0^{n+1}}{n+1} \tag{3.7}$$

where z_0 is the total wheel sinkage; and:

$$W = -b \int_0^{z_0} \left(\frac{k_c}{b} + k_\phi \right) z^n \, dx \tag{3.8}$$

In Eq. 3.7 the physical meaning is the force needed to compact the soil underneath the wheel, also referred to as compaction resistance R_c. this quantity can be calculated by deriving the dissipated work to sink (i.e. to compact) the wheel over a depth of z_0. In Eq. 3.8 x needs to be expressed in wheel dimension and wheel sinkage. For this derivation small wheel sinkages of $z_0 < D/6$ are assumed and a series expansion approximation is performed which means only accurate results are present for $n < 1.3$. The exact derivation can be found in [12]. Thus, Eq. 3.8 then yields after rearranging for z_0:

$$z_0 = \left(\frac{3W}{b(3-n)(k_c/b + k_\phi)\sqrt{D}} \right)^{2/(2n+1)} \tag{3.9}$$

where D is the wheel diameter. Consequently, the compaction resistance can be explicitly expressed by substituting Eq. 3.9 into Eq. 3.7 yielding, finally, a rather lengthy equation:

$$R_c = \frac{1}{(3-n)^{(2n+2)/(2n+1)}(n+1)b^{1/(2n+1)}(k_c/b + k_\phi)^{1/(2n+1)}} \left(\frac{3W}{\sqrt{D}} \right)^{(2n+2)/(2n+1)} \tag{3.10}$$

Traction

The other part of the drawbar pull equation (Eq. 3.1) is the generated thrust F. The thrust is limited by either the power of the motor which drives the wheel or by the traction that can be generated by the surface. For this application it is assumed that the motor is powerful enough, which means the thrust is limited by the soil, referred to as soil thrust H. This is quantified by the Mohr-Coulomb law, which describes the the maximum shear strength of a soil [12]:

$$\tau_{max} = c + \sigma \tan\phi \tag{3.11}$$

where τ_{max} is the maximum shear strength of the soil, c is the Coulombian coefficient of cohesion and ϕ is the Coulombian angle of internal friction of the soil. Accordingly, the maximum soil thrust is as follows:

$$H = A\tau_{max} = A(c + \sigma \tan\phi) = \underbrace{Ac}_{\text{Cohesion}} + \underbrace{W \tan\phi}_{\text{Friction}} \tag{3.12}$$

where A is the ground contact area. This equation is referred to as the Bernstein-Bekker equation, where it is assumed that no slip is present and the shear strength is constant.

Drawbar pull and assumptions

Now the motion resistances and traction are derived, these quantities can be subsituted into Eq. 3.1 yielding the semi-empirical prediction of the drawbar pull according to the Bekker model:

$$DP = Ac + W\tan\phi - bk\frac{z_0^{n+1}}{n+1} \tag{3.13}$$

Above equation is compactly written, seeing that Eq. 3.9 needs to be substituted for the total sinkage z_0.

In such manner the governing equation (Eq. 3.13) for the mobility of a wheeled vehicle on homogeneous granular soil is derived. With the calculated drawbar pull one knows how much force is left to overcome slopes, apparent obstacles or a region where the motion resistance of the soil is larger. As noticed, the Bekker model brings some assumptions and limitations with it. It is important to be aware of these and therefore they are summed up once more:

- *Radial normal stress*: Bekker assumed that the ground contact pressure is always perpendicular to the wheel surface.

- *Stress over width*: It is assumed the normal stress is constant in the direction of the wheel width.

- *Moderate sinkage*: the model is only accurate for moderate sinkages with $z_0 < D/6$.

- *Large diameter*: the model is only accurate for large diameters with $D/6 > z_0$.

- *Series expansion*: for formulating Eq. 3.9 the first two terms of a series expansion are used. This way the model is only accurate for exponentions of soil deformations of $n < 1.3$.

- *Constant shear stress*: it is assumed that the shear stress is constant over the surface of the wheel.

- *No slip*: it is assumed no slip is present. So the actual velocity is equal to the wheel-ground-interface velocity.

3.1.2. Modifications of the Bekker theory

By going through the Bekker model in previous section, one understands the basic principles of terramechanics theory. However, it brings some assumptions with it and it has turned out that it has quite some limitations, as mentioned before. In this section relevant improvements by superseding these assumptions and extensions to the desired application are described.

Pressure-sinkage relationship

In literature the pressure-sinkage relationship is oftenly called the backbone of terramechanics. A lot of parameters depend on this equation. Bekker based his version (3.2) on the Bernstein-Goratchkin equation (Eq. 3.3) and separated the sinkage component k into a cohesion and friction part. Reece however, came with an improvement [16] in 1965 inspired by the Terzaghi's soil bearing capacity theory [17]:

$$\sigma = \left(ck_c' + \gamma bk_\phi'\right)\left(\frac{z}{b}\right)^n \tag{3.14}$$

where γ is the weight density of the soil and non-dimensional pressure-sinkage parameters k_c' and k_ϕ' are equal to to Meyerhoff's soil bearing capacity factors N_c and N_γ, respectively. The major improvement of Reece's model is the dependence of the plate width b. Moreover, the non-dimensional k_c' and k_ϕ differ from Bekker's moduli, which are a function of n. This eases the analysis, because the moduli are explit this way. Ishigami built forth on Reece's model by improving the shape of the normal stress distribution [18]. The exit angle in this model is not at the dead point anymore, but is the same as the entrance angle, as can be seen in Fig. 3.2.

$$\sigma(\theta) = \left(ck_c' + \gamma bk_\phi'\right)\left(\frac{r}{b}\right)^n (\cos\theta - \cos\theta_1)^n \tag{3.15}$$

where θ_s is the static wheel-soil contact angle and the total sinkage is provided as:

$$z_0 = r(\cos\theta - \cos\theta_1) \tag{3.16}$$

The maximum stress is in front of the wheel instead of at the dead point of the wheel. Besides, the soil exit angle is behind instead of at the dead point. The semi-elliptical stress distribution is shown in Fig. 3.2. In recent literature the Ishigami model is mostly used.
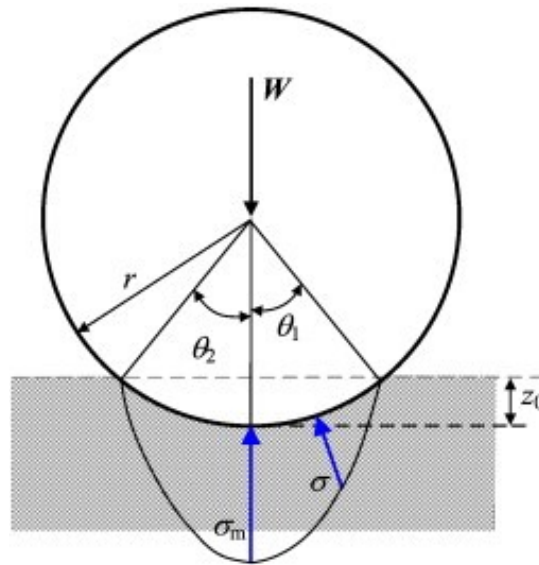
Figure 3.2: Normal stress distribution according to the Ishigami model.
Figure retrieved from [19].

Additional resistances

In most research publications, only the compaction resistance is taken into account (Eq. 3.10) because it is much more dominant than other motion resistances. However, in some cases other resistances could play a significant role.

Another type of motion resistance for a ground vehicle is bulldozing resistance. During driving, loose soil is pushed in front of the wheels and counteracts in the direction of motion. This resistance could be significant for loose soils and is described by [13]:

$$R_b = \frac{b\sin(\alpha+\phi)}{2\sin\alpha\cos\phi}(2zcK_c + \gamma z^2 K_\gamma) + \frac{\pi t^3 \gamma(90-\phi)}{540} \qquad (3.17a)$$

$$K_c = (N_c - \tan\phi)\cos^2\phi \qquad (3.17b)$$

$$K_\gamma = \left(\frac{2N_\gamma}{\tan\phi} + 1\right)\cos^2\phi \qquad (3.17c)$$

$$t = z\tan^2\left(45 - \frac{\phi}{2}\right) \qquad (3.17d)$$

$$\alpha = \cos^{-1}\left(1 - \frac{2z}{D}\right) \qquad (3.17e)$$

with R_b the bulldozing resistance, b the smaller dimension of the contact patch, α the angle of approach, ϕ the Coulombian angle of internal friction, z the sinkage, c the Coulombian coefficient of friction, K_c the modulus of cohesion of soil deformation, γ the specific weight of the soil, K_γ the modulus of density of soil deformation, t the distance of rupture, D the wheel diameter and N_c and N_γ the Terzaghi's bearing capacity factors in general shear failure, which can be obtained as reported in Ref. [17].

The motion is also resisted by the deformation of the wheel, the rolling resistance. The rolling resistance is then described by the following equation [13]:

$$R_r = fW \qquad (3.18)$$

with R_r the rolling resistance, f the coefficient of rolling resistance and W the vertical load acting on the wheel. When using flexible instead of rigid wheels, this resistance could be significant enough to include in the analysis.

Obviously, when dealing with slopes, the resistance experienced by gravition has to be taken into account:

$$R_g = W \sin \eta \tag{3.19}$$

with η is the angle of inclination.

Small wheels

Bekker's model for wheels is based on the assumption of a flat plate. The pressure-sinkage relationship and its coefficients are all derived from flate plate measurements. Bekker himself also noted this [13]:

"Predictions for wheels smaller than 20 inches in diameter become less accurate as wheel diameter decreases, because the sharp curvature of the loading area was neither considered in its entirety nor is it reflected in bevameter tests"

In other words, his model is only accurate for large wheels such that the contact area is approximately flat, like a plate. This originated from the Bernstein-Goratchkin equation (Eq. 3.3), the pressure-sinkage where the Bekker model is based on. As mentioned in section 3.1.1 Bekker states that his model is accurate for large wheels experiencing modest sinkage with $D/6 > z_0$. For small wheel diameters [20] constructed another semi-empirical model by fitting a diameter dependent exponent on experimental results:

$$\sigma = \hat{k} z^{\hat{n}} D^{\hat{m}} \tag{3.20}$$

where $\hat{m}$ is the diameter exponent, of which the value depends on the soil. Its is negative for compactive and positive for dilative soils for example. $\hat{k}$ and $\hat{n}$ are physically similar as k and n in Eq. 3.3, but have other dimensions. Their values are obtained with the same methodology.

After following the same procedure as described in section 3.1.1, the sinkage and compaction resistance are:

$$z_0 = \left(\frac{3W}{b(3-\hat{n})\hat{k} D^{\hat{m}+0.5}} \right)^{2/(2\hat{n}+1)} \tag{3.21}$$

$$R_c = b\hat{k} D^{\hat{m}} \frac{z_0^{\hat{n}+1}}{\hat{n}+1} \tag{3.22}$$

Wheel width

Meirion-Griffith and Spenko also noticed that the pressure-sinkage relation, and thus the drawbar pull, is dependent on the wheel width. They extended the diameter dependent model (Eq. 3.23) by including the width. The equation, applicable for compactive soils, for the sinkage then yields [21]:

$$z_0 = \left(\frac{3W}{b(3-\hat{n})\hat{k} \left(b\sqrt{Dz_0 - z_0^2} \right)^{\hat{m}+0.5}} \right)^{2/(2\hat{n}+1)} \tag{3.23}$$

The authors showed that the effects of D and b are independent on each other. It must also be noted that the sinkage equation does not have a closed form solution anymore, since z_0 is now a function of itself.

Slip and shear stress

As mentioned, Bekker assumes the shear strength acting on the wheel by the soil is constant. However, its distribution varies over the wheel perimeter because of slip. This implies that the shear stress changes; consequently the soil thrust and drawbar pull change. This improvement is described by the Janosi-Hamoto equation [22]:

$$\tau(\theta) = \tau_{max} \left(1 - e^{-j/\kappa} \right) = \left(c + \sigma(\theta) \tan \phi \right) \left(1 - e^{-j(\theta)/\kappa} \right) \tag{3.24}$$

where s is the slip ratio, j is the soil deformation and κ is the soil shear deformation modulus. The shear stress distribution is depicted in Fig.3.3 along with the normal stress distribution as described by Eq. 3.16. The wheel slip ratio is defined as:

$$s = \frac{r\omega - V}{r\omega} = 1 - \frac{V}{r\omega} = 1 - \frac{V}{V_t} \tag{3.25}$$

where ω is the angular speed, V is the actual speed and V_t is the theoretical speed. When a wheel experiences slippage the actual traveling velocity of the wheel is smaller than the theoretical velocity, the track speed. The slip ratio describes the percentage of that's left of the theoretical velocity which is created by the motor axle.

With the slip determined, one can calculate the soil deformation, which is the following for a wheel without grousers:

$$j(\theta) = r(\theta_1 - \theta - (1-s)(\sin\theta_1 - \sin\theta)) \tag{3.26}$$

Thus, in contrast to Eq. 3.12, where the shear stress is assumed constant, the soil thrust can be calculated by subsituting Eq. 3.24 for $\tau(\theta)$:

$$H = A\tau(\theta) = rb\int_{\theta_2}^{\theta_1} \tau(\theta)\cos\theta\,d\theta \tag{3.27}$$

From the shear stress the wheel torque can also be computed. The direction of the shear is tangential with respect to the wheel surface. This way it is perpendicular to the radius, the arm of the torque. Consequently, the torque is easily computed by multiplying the resulting shear force (shear stress times area) with the wheel radius:

$$T = r^2 b\int_{\theta_2}^{\theta_1} \tau(\theta)\,d\theta \tag{3.28}$$
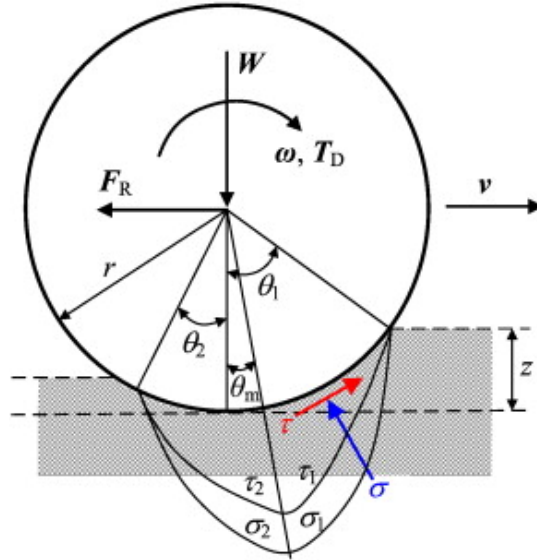

Figure 3.3: Soil stress distributions on a moving rigid smooth wheel.
Figure retrieved from [15].

Contribution of shear stress vertically

Bekker noticed that Eq. 3.5 was simplified in such way that the contribution of the shear stress is not taken into account. As can be seen in Fig. 3.3 the shear stress also includes a vertical component, which has part in the equilibrium in vertical direction:

$$-W + \sigma_z A + \tau_z A = 0 \tag{3.29}$$

where σ_z and τ_z are the vertical components of the normal and shear stress respectively, both dependent on angle θ. In Section 3.1.3 this will be elaborated further.

Slip and normal stress

The normal stress distribution changes when a wheel is in dynamic operation because of slip. In practice this results in a higher total sinkage. The Wong-Reece model [23] takes this into account by placing the point

of maximum of slip in front of the wheel's dead point by alternating Eq. 3.16 and yielding the following piecewise function:

$$\sigma(\theta) = \begin{cases} \sigma_1 = \left(\frac{k_c}{b} + k_\phi\right) z_1^n, & \theta_m < \theta < \theta_1 \\ \sigma_2 = \left(\frac{k_c}{b} + k_\phi\right) z_2^n, & \theta_2 < \theta < \theta_m \end{cases}$$

$$z_1 = r(\cos\theta - \cos\theta_1)$$

$$z_2 = r\left(\cos\left(\theta_1 - \frac{\theta - \theta_2}{\theta_m - \theta_2}(\theta_1 - \theta_m)\right) - \cos\theta_1\right) \tag{3.30}$$

where θ_m is the angle at which the maximum normal stress occurs, θ_f is the soil entry angle and θ_r is the soil exit angle. The stress distribution and its angles is graphically represented in Fig. 3.3. The equations to estimate these wheel-terrain interaction angles are:

$$\theta_1 = \arccos(1 - z/r) \tag{3.31a}$$

$$\theta_2 = c_3\theta_1 \tag{3.31b}$$

$$\theta_m = (c_1 + c_2 s)\theta_1 \tag{3.31c}$$

where c_1, c_2 and c_3 are the coefficients of wheel-soil interaction. In many cases c_3 is assumed to be zero. So from this equation it is seen that the normal stress distribution is dependent on slip by the position of the maximum stress. However, [24] noticed that not only the position of the maximum, but also the shape of the normal stress is variable when considering slip. Instead of the constant exponent of soil deformation n, a variable exponent N is used, which is a function of slip:

$$N = n_0 + n_1 s \tag{3.32}$$

with n_0 and n_1 the coefficients for calculating the sinkage component N.

Grousers
The profile of the current leg design of the Lunar Zebro is formed by grousers, as can be seen in Figure **??**. Compared to Eq. 3.12, grousers provide an extra contribution to the traction of a wheel H' [13]:

$$H = Ac + W\tan\phi + H' \tag{3.33}$$

For a detailed description on this subject, please consult [15] and [24].

3.1.3. Governing equations
In the past sections a lot of improvements and extensions on the Bekker theory are presented. In this section an overview and the general equations will be given, where every problem can be started with.

The governing equations for the wheel-soil interaction model are derived from static equilibrium in vertical (Eq. 3.34a) and horizontal (Eq. 3.34b) direction:

$$W = rb\int_{\theta_2}^{\theta_1} \underbrace{(\sigma(\theta)\cos\theta + \tau(\theta)\sin\theta)}_{\text{Normal force } N}\,d\theta \tag{3.34a}$$

$$DP = rb\int_{\theta_2}^{\theta_1} (\underbrace{\tau(\theta)\cos\theta}_{\text{Soil thrust } F} - \underbrace{\sigma(\theta)\sin\theta}_{\text{Resistance } R})\,d\theta \tag{3.34b}$$

The problem can be solved because these two equations have two unknowns: sinkage z (present in normal stress σ) and desired drawbar pull DP. First Eq. 3.34a is used to compute z. Then, z can be substituted into Eq. 3.34b for σ and τ, and finally the drawbar pull can be computed resulting in a measure of the vehicle performance.

So the variability of Eq. 3.34 is present in $\sigma(\theta)$ and $\tau(\theta)$ from the two fundamental relations: the pressure-sinkage relationship and the shear stress-shear displacement relation. In literature there is generally consensus about the use of the Janosi-Hamoto relationship (Eq. 3.24) for the latter, whereas there is a lot of variation

in the use of the pressure-sinkage relationship. For different applications different pressure-sinkage realtionships, and thus different normal stress profiles, apply (section 3.1.2).

In short, the main issue of attention is the pressure-sinkage relationship (normal stress distribution), because for the shear stress the Janosi-Hanamoto relationship is used in every problem. It must also be noted that this equation is dependent on the normal stress, from where the governing equations (Eq. 3.34) in practice will be a function of the normal stress profile after all.

3.2. Experimental set-up

An experimental set-up was elaborated and a simplified set-up was built. In this section its considerations are findings are presented. As mentioned in Chapter 2 only the traction was investigated and the goal was to validate the leg shape optimization results experimentally, and to evaluate the validity of the classical wheel model on legs. The set-up needed to be able to measure the drawbar pull and sinkage of a single leg.

In literature several researchers, among which Agarwal et al. [25], Iagnemma [24] and Meirion-Griffith and Spenko [20], developed a set-up for wheels. These set-ups are meant for dynamic measurements including slip, whereas this work focuses on a static situation.

In order to test the static tractive performance of a leg, the maximum soil thrust H must be measured; i.e. the horizontal force just before slippage. Fig. 3.4 shows the three configurations to measure this: a fixed leg with the horizontal force applied to the ground (Fig. 3.4a), a fixed ground with the horizontal force applied on the leg axle (Fig. 3.4b) and a fixed ground with a torque applied whereafter H is determined by the horizontal equilibrium (Fig. 3.4c). The former is unsuitable because the ground's mass is moved resulting in a large inertia and an overshoot after slippage. The third configuration is found to be less suitable than the second because the tractive effort is determined indirectly (by measuring the torque). Summarily, the configuration of Fig. 3.4b with the horizontal force applied on the leg axle is selected. Also, the motion resistance R needs to be measured to determine the drawbar pull DP. As the leg is in static state, this cannot be measured directly. As a result, the leg sinkage must be measured and substituted into Eq. 3.7 to determine R. Finally the drawbar pull can be determined: $DP = H - R$.

(a) Fixed leg, force applied

(b) Fixed ground, force applied
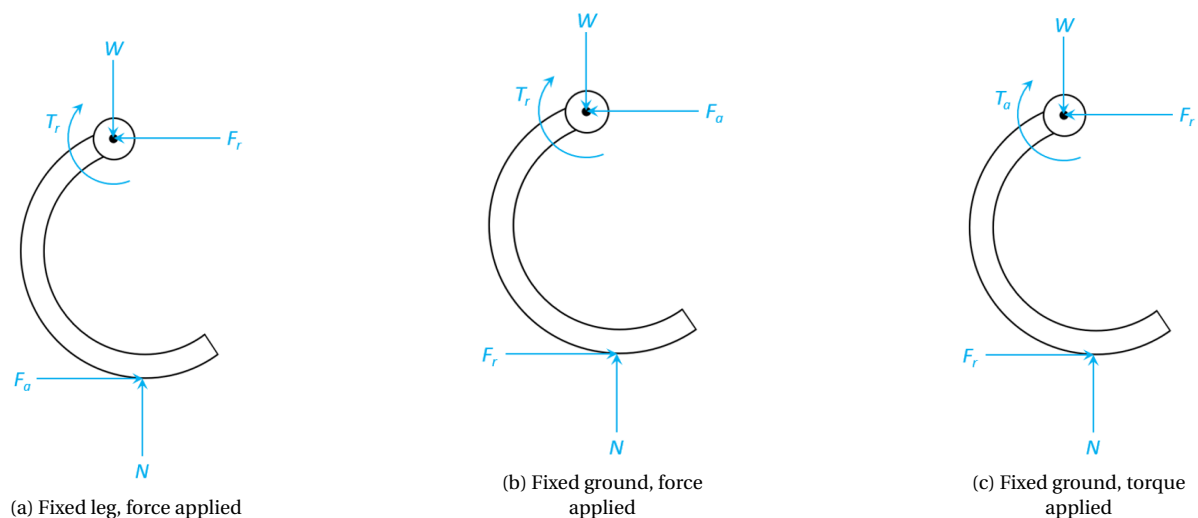
(c) Fixed ground, torque applied

Figure 3.4: Free body diagrams of static experimental set-up. Subscripts 'a' and 'r' denote applied and reaction forces, respectively.

A conceptual set-up, similar to the aforementioned references, is designed with degrees of freedom in the x- and z-direction, but the motor rotating the wheel/leg is not present due to the static measurement. Instead, the leg angle can be tuned and fixed. Fig. 3.5 shows the concept of the set-up to measure the drawbar pull of different leg shapes.

This set-up is not finalized during this project, but a simplified version is built to test the order of magnitude of the soil thrust, shown in Fig. 3.6. The horizontal force is increased by adding salt grains to the cup. The gravitational force is transferred by the pulley to the leg pendulum. When the leg slips, the weight addition is stopped. Finally the weight of the cup is measured resulting in the maximum soil thrust. The normal weight

can be adjusted by adding weight to the axle.

This set-up has its inaccuracies like the overshoot of the added weight by the reaction time of the executor. Also, moment of slip is not accurately detected. Additionally, there are losses present in the bearings of the pulley and the pendulum. Lastly, the preparation of the soil (loosening and smoothing) is not constant. Also the soil bin dimensions must be large enough so that the walls do not interfere with the normal stress profile. Reasonable dimensions can be calculated with Terzaghi's bearing capacity theory for shallow foundations [17].

In short, the simplified set-up measures the order of magnitude of maximum soil thrust H. In order to measure the drawbar pull DP (more accurately) the set-up of Fig. 3.5 should be elaborated and built.
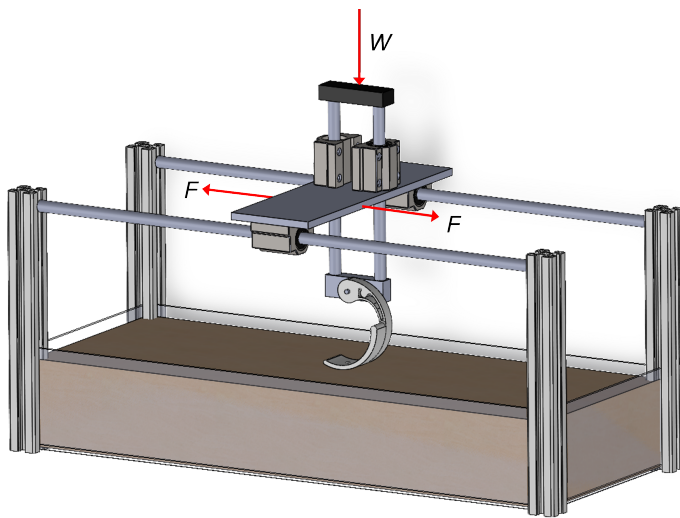

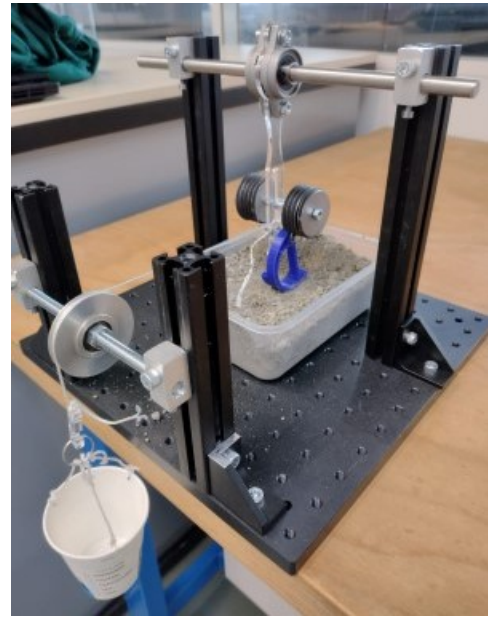Figure 3.5: Concept of experimental set-up to measure drawbar pull DP.

Figure 3.6: Simplified experimental set-up to measure soil thrust H.

3.3. Gravity

Gravity is an interesting physical parameter for the wheel-soil interaction on the Moon. In literature there is quite some contradiction on this subject for lightweight rovers, which would have low-gravity effects. In particular, the sinkage observed when regolith soil layers collapse under a normal wheel load has stirred the debate in the field of terramechanics. In 2019, Lopez-Arreguin et al. [26] noticed this contradiction and investigated this with the use of (newer) high accuracy terramechanics models [15] by reinterpretating the experimental results [27].

Before providing the opposing insights, the physics is explained. As explained in Chapter **??** the sinkage, the wheel penetration distance into the soil, is the most decisive parameter that directly influences the mobility of a rover. In literature this parameter is used as a measure to observe the influence of gravity on the mobility of rovers. The total sinkage z consists of two parts: the static sinkage z_0, when the wheels are stationary, and the dynamic sinkage z_d, when the wheels are in permanent rotation. [26] and [27] concluded that two competing physical effects determine the sinkage in lower gravities: Reduced Normal Load (RNL) and Reduced Bearing Capacity (RBC). The RNL effect describes the fact that, due to the lower gravity, the soil experiences a lower normal force causing the wheels to sink less. The RBC effect describes the fact that the confinement stress of the soil is reduced at lower gravities, diminishing the bearing capacity the granular material can endure leading to more sinkage [28].

Depending on the ratio of the magnitude of both effects, it can be concluded whether the sinkage is decreased, equal or increased in partial gravities. On the one hand [27] performed an experimental study during different parabolic flights, where partial gravities can be realized. He claimed that the amount of sinkage

changes insignicantly under a variable gravity, because the RNL and RBC effects practically cancel each other out. On the other hand, [28] and [29] suggest rover wheels could display worst sinkage performance in lower gravity fields than Earth, because the RBC effect would be more dominant than the RNL effect.

[26] reinterpretated the results of [27] and used more accurate models [15] [29]. It was concluded that the dynamic sinkage is larger under partial gravities, because the RBC effect is more dominant under low gravities than [27] thought. This fulfills the observations from [28], in a way that when rotated, wheels could slip more in low G's due to the poor soil strength with decreased gravity.

However, this claim is based on wheels with grousers. Contrarily, the authors pose that wheel sinkage differs not to little at different gravities for wheels with a smooth tread. In practice this is quite irrelevant, because UGVs will always contain a profile.

4

Matlab code

A lot of different analyses are performed during the thesis work. Here the main analysis is shown (Section 4.4 of the paper). All of the additional matlab scripts are attached.

4.1. Input parameters

```
1  % filename: Parameters_general
2  g = 1.635;           % gravitational acceleration [m/s^2]
3  m = 2.5;             % vehicle mass [kg]
4  b = 0.02;            % leg width [m]
5  c = 520;             % cohesion coefficient [Pa]
6  phi = 42;            % internal friction coefficient [deg]
7  k_c = 1400;          % cohesion modulus [Pa/m^{n-1}]
8  k_phi = 820000;      % friction modulus [Pa/m^n]
9  n = 1                % sinkage exponent [-]
10 y_b = 0.05;          % body height [m]
```

4.2. Analysis

```
1  % filename: Analysis_general
2  function [E_d,DP,h_c]=...
3  Analysis_general(g,m,b,r,k_c,k_phi,n,offset,y_b,phi,c);
4
5  %% Traction
6  k = k_c/b + k_phi;              % sinkage modulus
7  W = (m/2)*g;                    % normal force per leg
8  phir = phi*(pi/180);           % friction angle in radians
9
10 % Bekker n = 1
11 fun = @(theta1) k*b*r^2*(theta1-cos(theta1)*sin(theta1)) - W; % vertical equilibrum
12 theta1 = fzero(fun, 0.5);                         % numerical appr. of
       solution of theta1
13
14 % Numerical integration of stress profiles to determine H and R
15 ai = 0;
16 bi = theta1;
17 ni = 500;
18 hi = (bi-ai)/ni;
19 ii = 1:1:ni-1;
```

```matlab
20  fH=@(q) r.*b.*(c + (k.*r.^n.*(cos(q)—cos(theta1)).^n)*tan(phir)).*cos(q);     % Bekker
21  SiH = fH(ai+ii.*hi);
22  H = 2*double((hi./2).*(fH(ai)+fH(bi)+2.*sum(SiH)));                % Maximum soil thrust
23  fR=@(q) r.*b.*(k.*r.^n.*(cos(q)—cos(theta1)).^n).*sin(q);          % Bekker
24  SiR = fR(ai+ii.*hi);
25  R = double((hi./2).*(fR(ai)+fR(bi)+2.*sum(SiR)));                  % Motion resistance
26
27  DP = H—R;                                                          % Drawbar pull
28
29
30  %% Mobility
31  alfa = linspace(0*pi,1.75*pi,500);        % leg angle [rad]
32  h = 3;                                    % number of leg instances
33  y_o = r — offset;            % vertical CoR offset
34  rho = r;                     % general radius
35  x0 = rho*sin(alfa) + x_o;    % horizontal coordinate starting configuration
36  y0 = —rho*cos(alfa) + y_o;   % vertical coordinate starting configuration
37  p0 = [x0 ; y0];              % coordinate on leg, for hip on origin
38
39  theta_h = real(acos((r—y_b)/(r—offset)));   % rotation touch angle
40  alfa_min_h = theta_h;        % leg touch angle
41
42  theta = linspace(theta_h,2*pi—theta_h,h);   % rotation angle
43
44  for j=1:1:length(theta)
45      Ri(:,:,j) = [cos(theta(j)) sin(theta(j));—sin(theta(j)) cos(theta(j))]; % rotation
            matrix, clockwise
46      x(:,j) = Ri(1,:,j)*p0;           % horizontal coordinate rotated configuration
47      y(:,j) = Ri(2,:,j)*p0 + y_b;     % vertical coordinate rotated configuration,
            vertical offset due to body thickness
48      [y_min(:,j),I(:,j)] = min(y(:,j)); % vertical minimum + index
49      alfa_min(j) = alfa(I(j));        % leg angle of vertical minimum
50      x_c0(j) = x0(I(j));              % contact point hor.
51      y_c0(j) = y0(I(j));              % contact point vert.
52      c0 = [x_c0 ; y_c0];              % contact point on leg, for hip on origin (theta =
            0)
53      x_c(j) = Ri(1,:,j)*c0(:,j);      % contact point hor., rotated configuration
54      y_c(j) = Ri(2,:,j)*c0(:,j);      % contact point vert., rotated configuration
55
56      x_t(j) = r*(abs(alfa_min(j))—abs(alfa_min_h)) — x_c(j) + (r—offset)*sin(theta_h);
57      y_t(j) = —y_c(j) — y_b;
58      CoR_x_g(j) = x_t(j);             % x—coordinate hip
59      CoR_y_g(j) = y_b + y_t(j);       % y—coordinate hip
60      x_g(:,j) = x(:,j) + x_t(j);      % horizontal coordinate
61      y_g(:,j) = y(:,j) + y_t(j);      % vertical coordinate
62  end
63
64  x_h = CoR_x_g;                       % Horizontal hip position
65  y_h = CoR_y_g;                       % Vertical hip position
66
67  x_total = max(x_h);                  % Distance covered per cycle
68  x_total = 2*(pi—theta_h)*r + 2*(r—offset)*real(sin(theta_h));
69
70  % Potential energy
71  % V_y = (m/3)*g*y_h;                           % Gravitional potential energy
72  % V_y_c = max(V_y) — V_y(1);          % Consumed energy per cycle
```

```matlab
73  V_y_c = (m/3)*g*(2*r — offset — y_b);    % Consumed energy per cycle
74
75  % Compaction work
76  E_R = R*x_total;
77
78  % Distance covered per Joule
79  if V_y_c < 0.0001
80      E_d = inf;
81  else
82      E_d = x_total/(V_y_c + E_R);
83  end
84
85
86  %% Climbing
87  z = r*(1—cos(theta1));                % sinkage
88  h_c = 3*r — 2*offset — z;             % climbing height
89  end
```

4.3. Performance output

```matlab
1   % filename: Output_general
2   close all, hold off, clear
3
4   % Assignment of constant design parameter values
5   Parameters_general;
6
7   % Output of design variables:
8   r = linspace(0.025,0.06,1000);        % Leg radius [m]
9   offset = linspace(0,0.05,1000);       % CoR offset [m]
10
11  for j=1:1:length(offset)
12    for i=1:1:length(r)
13      [E_d,DP,h_c]=...
14      Analysis_general(g,m,b,r(i),k_c,k_phi,n,offset(j),y_b,phi,c);
15      funE_d(j,i) = E_d;
16      funDP(j,i) = DP;
17      Fun(j,i) = h_c;
18    end
19  end
```

Bibliography

[1] J. B. Miog, "Design of the locomotion subsystem for Lunar Zebro," 2018.

[2] L. Z. Structures, "Structures & Thermal Sub - System – Lunar Zebro."

[3] U. Saranli, M. Buehler, and D. E. Koditschek, "RHex: A simple and highly mobile hexapod robot," *International Journal of Robotics Research*, vol. 20, no. 7, pp. 616–631, 2001.

[4] G. H. HEIKEN, D. T. VANIMAN, and B. M. FRENCH, "Lunar Sourcebook," *Cambridge University Press*, p. 778, 1991.

[5] R. Exploration, *PLANETARY*.

[6] E. N. Slyuta, "Physical and Mechanical Properties of the Lunar Soil (A Review)," vol. 48, no. 5, pp. 330–353, 2014.

[7] U. Jahn, D. Heß, M. Stampa, A. Sutorma, C. Röhrig, P. Schulz, and C. Wolff, "A taxonomy for mobile robots: Types, applications, capabilities, implementations, requirements, and challenges," *Robotics*, vol. 9, no. 4, pp. 1–24, 2020.

[8] L. Bruzzone and G. Quaglia, "Review article: Locomotion systems for ground mobile robots in unstructured environments," *Mechanical Sciences*, vol. 3, no. 2, pp. 49–62, 2012.

[9] A. Vina and A. Barrientos, "C-legged hexapod robot design guidelines based on energy analysis," *Applied Sciences (Switzerland)*, vol. 11, no. 6, 2021.

[10] M. F. Silva and J. A. MacHado, "A literature review on the optimization of legged robots," *JVC/Journal of Vibration and Control*, vol. 18, no. 12, pp. 1753–1767, 2012.

[11] ——, "A historical perspective of legged robots," *JVC/Journal of Vibration and Control*, vol. 13, no. 9-10, pp. 1447–1486, 2007.

[12] R. T. Sataloff, M. M. Johns, and K. M. Kost, *No Title*, 2001.

[13] M. Bekker, *Theory of Land Locomotion*, 1960.

[14] R. Bernstein, "Probleme zur experimentellen motorpflugmechanik," *Der Motorwagen*, vol. 16, 1913.

[15] L. Ding, Haibogao, YuankaiLi, GuangjunLiu, and ZongquanDeng, "Improved explicit-form equations for estimating dynamic wheel sinkage and compaction resistance on deformable terrain," *Mechanism and Machine Theory*, vol. 86, pp. 235–264, 2015. [Online]. Available: http://dx.doi.org/10.1016/j.mechmachtheory.2014.12.011

[16] B. A. R. Reece, B. Sc, and P. D. A. Member, "Principles of soil-vehicle mechanics," vol. 180, no. 2.

[17] K. Terzaghi, *Theoretical Soil Mechanics*, 1943.

[18] G. Ishigami, "Terramechanics-based analyis and control for lunar/planetary exploration robots," *PhD thesis*, vol. University, 2009.

[19] G. Meirion-griffith and M. Spenko, "A Comprehensive Pressure-Sinkage Model for Small-Wheeled Unmanned Ground Vehicles on Dilative , Deformable Terrain," pp. 4052–4057, 2012.

[20] ——, "A modified pressure – sinkage model for small , rigid wheels on deformable terrains," *Journal of Terramechanics*, vol. 48, no. 2, pp. 149–155, 2011. [Online]. Available: http://dx.doi.org/10.1016/j.jterra.2011.01.001

[21] ——, "A pressure-sinkage model for small-diameter wheels on compactive , deformable terrain," *Journal of Terramechanics*, vol. 50, no. 1, pp. 37–44, 2013. [Online]. Available: http://dx.doi.org/10.1016/j.jterra.2012.05.003

[22] Z. Janosi and B. Hanamoto, "Analytical determination of drawbar pull as a function of slip for tracked vehicle in deformable soils," *Proceedings of the 1st International Conference of Terrain Vehicle Systems*, 1961.

[23] J. Y. Wong and A. Reece, "PREDICTION OF RIGID WHEEL PERFORMANCE BASED ON THE ANALYSIS OF SOIL-WHEEL STRESSES PART I. PERFORMANCE OF DRIVEN RIGID WHEELS," 1967.

[24] K. D. Iagnemma, "Interaction Mechanics Model for Rigid Driving Wheels of Planetary Rovers Moving on Sandy Terrain with Consideration of Multiple Physical Effects," vol. 32, no. 6, pp. 827–859, 2015.

[25] S. Agarwal, C. Senatore, T. Zhang, M. Kingsbury, K. Iagnemma, D. I. Goldman, and K. Kamrin, "Modeling of the interaction of rigid wheels with dry granular media," *Journal of Terramechanics*, vol. 85, pp. 1–14, 2019.

[26] A. J. Lopez-Arreguin, B. Gundlach, and E. Stoll, "Do lunar rover wheels sink equally on Earth and Moon?" *Results in Physics*, vol. 15, no. March, p. 102617, 2019. [Online]. Available: https://doi.org/10.1016/j.rinp.2019.102617

[27] T. Kobayashi, Y. Fujiwara, J. Yamakawa, N. Yasufuku, and K. Omine, "Mobility performance of a rigid wheel in low gravity environments," *Journal of Terramechanics*, vol. 47, no. 4, pp. 261–274, 2010. [Online]. Available: http://dx.doi.org/10.1016/j.jterra.2009.12.001

[28] M. Jiang, F. Liu, Z. Shen, and M. Zheng, "Distinct element simulation of lugged wheel performance under extraterrestrial environmental effects," *Acta Astronautica*, vol. 99, no. 1, pp. 37–51, 2014. [Online]. Available: http://dx.doi.org/10.1016/j.actaastro.2014.02.011

[29] W. Li, Y. Huang, Y. Cui, S. Dong, and J. Wang, "Trafficability analysis of lunar mare terrain by means of the discrete element method for wheeled rover locomotion," *Journal of Terramechanics*, vol. 47, no. 3, pp. 161–172, 2010. [Online]. Available: http://dx.doi.org/10.1016/j.jterra.2009.09.002